Bachelor Project

Czech Technical University in Prague

F3

Faculty of Electrical Engineering
Department of Circuit Theory

# Comparison of methods for calculating coherence and cross-frequency coupling of brain oscillations in animal models

Jakub Benetin

Supervisor: RNDr. David Levčík, Ph.D.
Supervisor–specialist: Ing. Radek Janča, Ph.D.
May 2024

# BACHELOR‘S THESIS ASSIGNMENT

## I. Personal and study details

Student's name: **Benetin Jakub** Personal ID number: **507442**

Faculty / Institute: **Faculty of Electrical Engineering**

Department / Institute: **Department of Circuit Theory**

Study program: **Medical Electronics and Bioinformatics**

## II. Bachelor’s thesis details

Bachelor’s thesis title in English:

**Comparison of methods for calculating coherence and cross-frequency coupling of brain oscillations in animal models**

Bachelor’s thesis title in Czech:

**Srovnání metod výpočtu koherence a mezifrekvenční vazby mozkových oscilací u animálních modelů**

Guidelines:

Coherence and cross-frequency coupling are fundamental techniques in the analysis of brain activity, that allow them to reveal the synchronization of neuronal activity in different brain regions and the interaction between different brain oscillations. Coherence and cross-frequency coupling assessments are used to understand the connections between brain regions and to identify specific frequency patterns that may be associated with particular cognitive functions or pathological conditions. The aim of this thesis is to evaluate existing methods, emphasizing their accuracy, sensitivity and specificity for use on local field potentials (LFP) recordings in rodent models of neurological and psychiatric diseases.
1. Introduce the concept of coherence and cross-frequency coupling.
2. Implement/use algorithms to calculate coherence and cross-frequency coupling using Fourier, Hilbert, and wavelet transforms.
3. Validate the outputs of each technique on artificial data (e.g., noise sensitivity, temporal resolution).
4. Apply the techniques to real signals from animal experiments and try to select the most appropriate techniques.

Bibliography / sources:

[1] Nakhnikian, A., et al. "A novel cross-frequency coupling detection method using the generalized Morse wavelets." Journal of neuroscience methods 269 (2016): 61-73.
[2] Cheng, Ning, et al. "A precise annotation of phase-amplitude coupling intensity." Plos one 11.10 (2016): e0163940.
[3] Hülsemann, Mareike J., Ewald Naumann, and Björn Rasch. "Quantification of phase-amplitude coupling in neuronal oscillations: comparison of phase-locking value, mean vector length, modulation index, and generalized-linear-modeling-cross-frequency-coupling." Frontiers in neuroscience 13 (2019): 573.
[4] Tort, Adriano BL, et al. "Dynamic cross-frequency couplings of local field potential oscillations in rat striatum and hippocampus during performance of a T-maze task." Proceedings of the National Academy of Sciences 105.51 (2008): 20517-20522.

 

Name and workplace of bachelor's thesis supervisor:

**RNDr. David Levčík, Ph.D. Institute of Physiology CAS, Prague**

Name and workplace of second bachelor's thesis supervisor or consultant:

Date of bachelor's thesis assignment: **06.02.2024** Deadline for bachelor thesis submission: **24.05.2024**

Assignment valid until: **21.09.2025**

| RNDr. David Levčík, Ph.D.<br>Supervisor's signature | doc. Ing. Radoslav Bortel, Ph.D.<br>Head of department's signature | prof. Mgr. Petr Páta, Ph.D.<br>Dean's signature |
|---|---|---|

## III. Assignment receipt

The student acknowledges that the bachelor's thesis is an individual work. The student must produce his thesis without the assistance of others, with the exception of provided consultations. Within the bachelor's thesis, the author must state the names of consultants and include a list of references.

| . | |
|---|---|
| Date of assignment receipt | Student's signature |

 

# Acknowledgements

I would like to express my gratitude to RNDr. David Levčík, Ph.D. and Ing. Radek Janča, Ph.D. for supervising this work and offering much needed advice and guidance through the whole process. I also thank RNDr. David Levčík, Ph.D., and by extension, all his colleagues who took part in the recording sessions, for providing me with electrophysiological recordings.


# Declaration

I declare that I elaborated this thesis on my own and that I mentioned all the information sources and literature that have been used in accordance with the Guideline for adhering to ethical principles in the course of elaborating an academic final thesis.

In Prague, May 22, 2024

# Abstract

Coherence and cross-frequency coupling are fundamental techniques in the analysis of brain activity, that allow to reveal the synchronization of neuronal activity in different brain regions and the interaction between different brain oscillations. Coherence and cross-frequency coupling assessments are used to understand the connections between brain regions and to identify specific frequency patterns that may be associated with particular cognitive functions or pathological conditions.

The aim of this thesis is to evaluate several existing methods for detection of phase-amplitude coupling on simulated data, emphasizing their sensitivity to noise and time/frequency resolution. Namely I chose wavelet coherence, phase-locking value modulation index and mean vector length modulation index.

These methods were subsequently employed for analysis of local field potential recordings from parvalbumin-Cre transgenic mice, to examine possible changes in hippocampal theta-gamma phase-amplitude coupling after brain-wide chemogenetic activation of parvalbumin interneurons. Findings are so far inconclusive, due to small number of subjects (n = 4), but changes in hippocampal theta-gamma coupling were present across experimental conditions and warrant further study.



**Keywords:** Coherence, Cross-Frequency Coupling, Brain Oscillations, Animal Models, Signal Processing



**Supervisor:** RNDr. David Levčík, Ph.D.
Institute of Physiology CAS,
Vídeňská 1083,
142 00,
Praha 4



# Abstrakt

Koherence a mezifrekvenční vazba představují základní techniky v analýze mozkové aktivity, umožňující odhalit synchronizaci neuronální aktivity v různých oblastech mozku a vzájemnou interakci mezi různými mozkovými oscilacemi. Hodnocení koherence a mezifrekvenční vazby jsou využívány k porozumění propojení mezi mozkovými oblastmi a identifikaci specifických frekvenčních vzorů, jež mohou být spojeny s konkrétními kognitivními funkcemi či patologickými stavy.

Cílem této práce je zhodnotit několik stávajících metod pro detekci fázově-amplitudové vazby na simulovaných datech, se zaměřením na jejich citlivost na šum a časové/frekvenční rozlišení. Konkrétně jsem zvolil vlnkovou koherenci, phase-locking value modulation index a mean vector length modulation index.

Tyto metody byly následně použity pro analýzu elektrofyziologických záznamů z parvalbumin-Cre transgenních myší, a nalezení změn ve theta-gamma fázově-amplitudové vazbě po globální chemogenetické aktivaci parvalbuminových interneuronů. Zjištění jsou zatím neprůkazná kvůli malému počtu zvířat (n = 4), ale změny v hippokampální theta-gamma vazbě naskrz experimentálními podmínkami byly přítomny a zaslouží si další studium.



**Klíčová slova:** Koherence, Mezifrekvenční vazba, Mozkové oscilace, Animální modely, Zpracování signálů

**Překlad názvu:** Srovnání metod výpočtu koherence a mezifrekvenční vazby mozkových oscilací u animálních modelů

# Contents

# Figures

# Tables

## List of Abbreviations

**AAC** Amplitude-amplitude coupling

**AD** Alzheimer's disease

**CFC** Cross-frequency coupling

**CWT** Continuous wavelet transform

**DHT** Discrete Hilbert transform

**dHPC** Dorsal hippocampus

**ECoG** Electrocorticogram

**EEG** Electroencephalogram

**FFT** Fast Fourier transform

**LFP** Local field potential

**MI** Modulation index

**mPFC** Medial prefrontal cortex

**MVL MI** Mean vector length modulation index

**PAC** Phase-amplitude coupling

**PD** Parkinson's disease

**PFC** Phase-frequency coupling

**PPC** Phase-phase coupling

**PLV MI** Phase-locking value modulation index

**PV** Parvalbumin

**SNR** Signal-to-noise ratio

# Chapter 1

# Introduction

## 1.1 Neural Oscillations

Neural oscillations emerge due to the activity of neurons in the brain (and even in brain slices in vitro [1]). On long time scales, no clear spectral peaks appear, but for short time windows (seconds), power is concentrated around certain frequencies. Why this separation of power happens and what are the consequences has been a matter of interest since the invention of the electroencephalogram (EEG). Since then, measuring devices similar to EEG have been invented, namely the electrocorticogram (ECoG) [2] and electrodes for measuring local field potentials (LFP). Generally, oscillations appear in recordings from any of these methods. This is not surprising, since these record the electrical activity of the brain (extracellular voltage), but with different spatial resolution, see Figure 1.1.

Usual ranges of neural oscillations are listed in Table 1.1, however these are not sharply defined. Currently, since mechanisms that lead to them are not well understood, it is possible that certain rhythms will bear different designations across species, even if they fulfill similar roles (especially if they fall on the border of respective ranges). There is also variability in individuals of the same species, so labeling oscillations is done with some flexibility, see [3], [4].

Assigning functions and behavioral correlations to individual types of brain oscillations has proven beyond challenging and opinions are diverse. Some researchers even propose that neural oscillations are not a feature, but only a byproduct, which may be undesirable [5]. However, the prevailing view suggests that brain oscillations indeed have an important role, and evidence in support only grows each year. Examples will be presented below, with main focus on LFP data in later parts.

### 1.1.1 Proposed Functions and Roles

When there is a relation to certain function, it is hardly ever exact, and many things can only be suspected. Mentioned below are just some general findings in a very brief manner. For a longer account, reviews on each rhythm are cited in the beginnings of their respective paragraphs. It will be a recurring

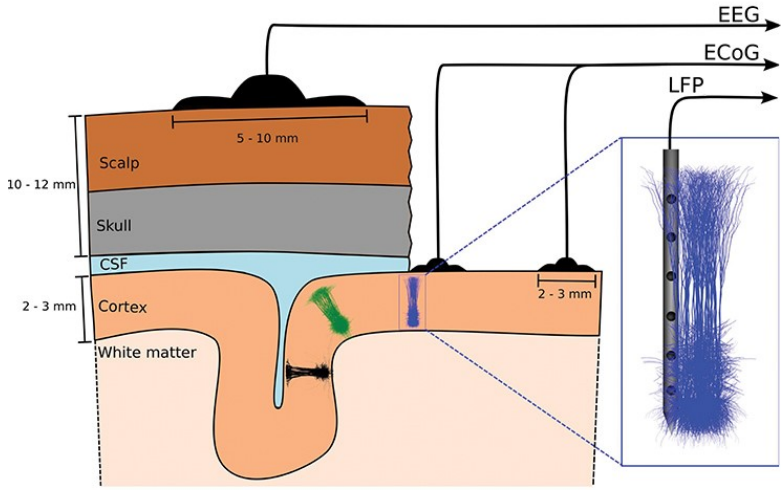


**Figure 1.1:** Recording sites for electrophysiological methods. EEG electrodes are placed on the scalp. Typically modern EEG caps have 32, 64, 128 or more individual electrodes. ECoG electrodes are placed either outside dura mater (not shown), or subdurally, directly on the exposed cortex. LFP electrodes are inserted into the tissue. Adapted from [6].

theme, that all neural oscillations are linked to a variety of processes. This is to be expected, since they appear throughout the entire brain, and thus likely contribute to many aspects of cognition.

**Delta** rhythm [7], [8], appears during sleep stages, particularly during deep sleep (slow-wave sleep). While it plays a crucial role in regulating sleep architecture and promoting restorative sleep patterns, its involvement in other cognitive processes is less well understood. Delta has been linked with decision making, mental calculation [9], object/word recognition and memory consolidation [10]. It has also been suggested as a mechanism of top-down control, where this slow rhythm inhibits brain circuits which are not necessary for the current task.

**Theta** rhythm [11], [12] has been linked to, spatial navigation, memory, motion and attention [13]. It is particularly generated in the hippocampus. For example, in rodents, large amplitude waves of 4-10 Hz appear when the animal starts to run, but remain some time even afterwards, when the animal stops. Another role also lies in sensory processing. Theta appears during activities when an animal perceives the enviroment, such as sniffing [4]. As for its role in memory, it is well estabilished that lesions on the hippocampus result in impaired episodic memory [14]. Memories are thought to be encoded and retrieved within certain phase of the hippocampal theta rhythm [15]. In support of this, Kerrén et al. report that theta phase at which memories are encoded and retrieved with highest accuracy are shifted by roughly

180 degrees [16].

**Alpha** [17], the first rhythm to be described, has been studied quite extensively in regards to attention. Generally, increase in alpha amplitude has been associated with decreased attention. Some researchers have also proposed it as an attentional suppression mechanism, where the alpha rhythm inhibits activity of neurons that would process irrelevant stimuli [18], since it is strong in cortical neurons not activated by a stimulus [19].

**Beta** rhythm [20] mainly originates from the sensorimotor cortex and basal ganglia in short bursts [21] [22]. It is uncertain whether these sources are independent of each other. Amplitude decreases prior to and during execution of movement and increases upon cessation. Beta activity is also enhanced during motor imagery, or while observing motion. This suggests there might be some functional similarities with alpha (especially on their border), since Fries also mentions it as a mechanism of top-down control [19]. I should also add, that what is referred to as alpha in the occipital region is sometimes referred to as the mu rhythm (from the alpha family) in the sensorimotor cortex, which is characteristic of an "idling" state [23].

**Gamma** [24], as traditionally defined, has the broadest frequency content. As such, it is common to further subdivide it into slow and fast gamma (30-70 Hz and 70-150 Hz respectively). Supposedly, gamma activity of neuronal assemblies reflects packets of information in a temporally coordinated fashion [23], [25]. As to how exactly information is encoded within these "packets", remains unclear. Nevertheless, gamma rhythm is linked to practically all forms of sensory information processing in the brain and it is usually modulated by the slower rhythms, like theta, in the process.

| Frequency Band | Human | Rodents |
|---|---|---|
| Delta | 0.5-4 Hz | 0.5-4 Hz |
| Theta | 4-8 Hz | 4-8 Hz |
| Alpha | 8-12 Hz | 8-13 Hz |
| Beta | 12-30 Hz | 13-30 Hz |
| Low Gamma | 30-70 Hz | 30-80 Hz |
| High Gamma | 70-150 Hz | 80-150 Hz |

**Table 1.1:** Approximate frequency ranges of neural oscillations in humans and rodents.

### 1.1.2 Origin of Neural Oscillations

In short, all ionic processes across various types of excitable membranes within the brain influence the LFP. Transmembrane current, regardless of its origin, contributes to both intracellular and extracellular voltage fluctuations. Synaptic activity is often the most significant source of extracellular current flow, since it lasts long enough for activity of many cells to overlap and lead

to measurable signals [26]. These synaptic currents involve neurotransmitters acting on synaptic receptors, leading to inward ion flow at the synapse, resulting in a local extracellular sink. To maintain electroneutrality, this sink is balanced by an extracellular source, termed passive or return current.

Additionally, various non-synaptic events contribute prominently to the extracellular field. Among these are action potentials, calcium spikes, intrinsic currents, and many others. Geometry of neurons also plays a significant role in their ability to generate dipoles and this determines, how strongly they contribute to the total electric field. Neurons with axial geometry, such as pyramidal neurons, have the ability to generate stronger dipoles [27], compared to neurons with a more spherical shape.

Many possible models have been developed to understand how certain types of cells (most basic distinction being inhibitory/excitatory) could be connected in order to generate these rhythms. For example, the gamma rhythm E-I or I-I models are mentioned in [28]. Thanks to optogenetics or pharmacological agents, it is possible to adjust the activity of neuronal populations. Silencing or increasing the activity of a particular type of neurons can yield further insight to which types of cells are integral to sustain some rhythms in vivo or in vitro.

For instance, thanks to these approaches, it is known today, that inhibitory interneurons are needed for the emergence of gamma oscillations. Namely parvalbumin-expressing (PV) interneurons generate these rhythms in the hippocampus and they have the ability to fire reliably and precisely in concert with other interneurons [25]. In another study, Amilhon et al. were able to disrupt hippocampal 8Hz theta by optogenetically silencing PV interneurons [29]. For longer account on hippocampal theta activity and possible interactions with gamma, see [11].

## 1.2 Communication through Coherence (CTC) Hypothesis

This hypothesis of P. Fries has garnered significant attention in neuroscience. The name comes from the coherence metric, which is used to calculate a degree of synchronization. For a full account, see the original paper [30] and the updated version [19]. Most of the investigation was carried out on the interaction of neurons from different layers of visual and motor cortex (typically of macaque monkeys).

In short, when a group of neurons is activated, they synchronize their activity. This creates rhytmic fluctuations in voltage, which leads to time windows of inhibition and excitation. Inputs which arrive at cycles of excitation will have much greater chance of making the receiving neuron fire (greater chance of the input being processed). Those that arive during inhibition will have little to no impact. Outputs of these neurons are inputs for another group of neurons. If these outputs arrive randomly, they are unlikely to be processed, so the sending and receiving groups must be synchronized for communication

to occur.

Such synchronization occurs even for fast gamma oscillations of distant connected neuronal groups. Even when the gamma frequency fluctuates, it does so in both groups in a similar manner [31]. Much more evidence in support is mentioned in the original papers.

## 1.3 Cross-Frequency Coupling (CFC)

CFC refers to the synchronization between the phases or amplitudes of neural oscillations at distinct frequencies. This phenomenon is supposed to play a central role in coordinating information processing across different brain regions and communication between brain areas. Most often mentioned types are described below and can be seen in Figure 1.2.

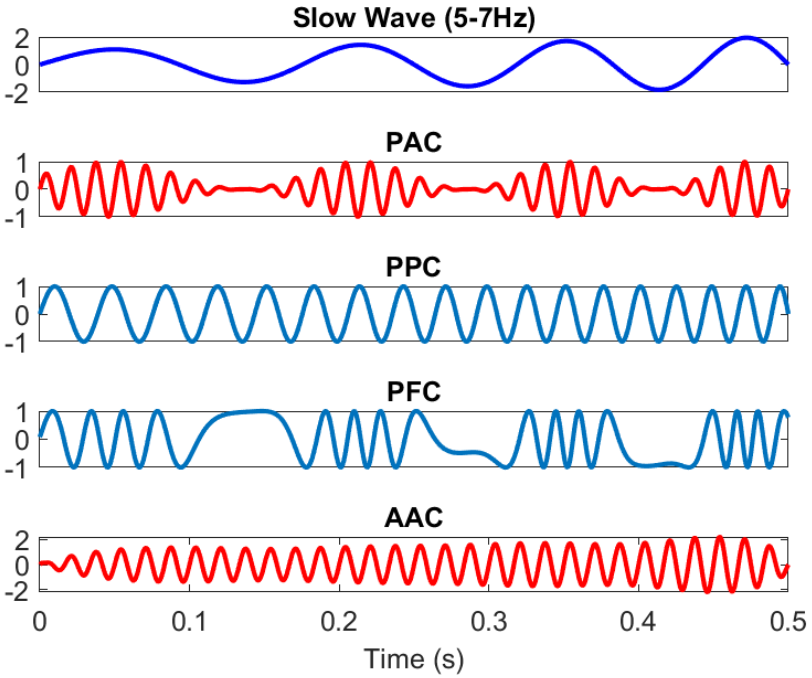


**Figure 1.2:** Illustration of CFC types. Slow wave (top) is gradually increasing in frequency and amplitude. Fast oscillations (plots below) are coupled to the slow oscillation in different ways.

**Phase-Amplitude Coupling (PAC)** has been examined extensively (review of PAC [32]). The slower rhythm is thought to recruit distant neuronal groups into assemblies and ensures they fire in a coordinated fashion. Reasoning for this assumption is that the increase in extracellular voltage at the peak of a slow oscillation greatly increases the spiking likelihood of all affected neurons by bringing them closer to their threshold potential. Things are not always so straightforward, and sometimes neurons fire at phase that does not correspond to the peak or trough. This has been attributed to

different conduction delays between upstream and downstream neurons, but other factors could play a role. Also, multiple slow rhythms can modulate high frequency power simultaneously [33]. This coupling is present in many brain regions, but most data comes from the cortex and hippocampus during working memory tasks and learning [34].

**Phase-Frequency Coupling (PFC)** is a type of coupling in which the phase of one oscillation modulates the frequency of another, presumably by modulating the excitability of neurons which give rise to the fast rhythm. It is unlikely that the slow wave would be able to modulate the frequency of the fast wave beyond certain range. This type of coupling is reported only rarely [35].

**Phase-phase coupling (PPC)** describes the alignment of the phases of two oscillatory signals over time [35]. It means that as one signal completes a cycle, the phase of the other signal coincides with certain points in that cycle. It is also called n:m coupling when the frequency of the faster oscillation is an integer multiple of the slower oscillation (1:5 in Figure 1.2). Whether true PPC occurs in the hippocampus (and other regions as well) has been called into question. Misleading coupling levels may result from the asymmetrical waveform or methods used for time-frequency analysis, such as filtering [36].

**Amplitude-Amplitude Coupling (AAC)** has been investigated and reported little in comparison. Which function it serves, if any, is uncertain [37]. Two fast waves can appear to have AAC when their amplitudes are simultaneously modulated by the phase of some slow rhythm.

In a recent paper, Gonzales et al. have examined the possible connection between CFC and the CTC hypothesis. Their findings have shown that the phase of theta waves influences fast gamma synchronization (100-150 Hz) across the neocortex during REM sleep. These results suggest a potential link between the phenomena of CTC and CFC, hinting at a unified mechanism for efficient long-range communication [38].

## 1.4 Neural Oscillation in Brain Disorders

One of the reasons for analyzing neural oscillations lies in understanding and diagnosing neurological/neuropsychiatric diseases [39]. The most outwardly obvious alterations in brain rhythms (and their couplings) arise in epilepsy. Other conditions such as Alzheimer's disease (AD), Parkinson's disease (PD) and schizophrenia are also extensively studied in this context [40].

In **AD**, the general trend in resting-state EEG is a decrease in power of higher (alpha, beta, gamma) and increase in slower frequencies (theta, delta). This change correlates with memory impairment [41]. Changes in coupling (particularly theta-gamma) have been reported in rat and mice models of

AD and that is even before noticeable memory impairments and increased concentrations of amyloid beta, a well estabilished marker of AD [42], [43].

**PD** is characterized by tremors, rigidity and bradykinesia (slowness of movement). The first two are related to changes in beta oscillations, while the tremors are coherent with theta oscillations (in unmedicated patients) [44], [45]. Abnormally high beta-gamma PAC appears in several brain areas related to motor function [46] (subthalamic nucleus, primary motor cortex, premotor cortex, primary somatosensory cortex, prefrontal cortex), and it is high also across these regions. Gong et al. showed that only coupling between different regions correlates with motor dysfunction [47]. Nevertheless, both serve as good markers of PD, and the latter may be an important avenue for further research.

In **schizophrenia**, EEG recordings show impaired theta-gamma PAC during working memory task [48]. Some studies were unable to distinguish significant differences in PAC, noting that it may be task-dependent [40]. Even when theta-gamma PAC is preserved, patients exhibit changes in power of most frequency bands. Most consistent among these are increased theta/delta power. Other frequency bands show changes that vary in individuals. Comparing greater number of patients is further complicated due to diverse treatment options, which can affect certain rhythms in virtually any metric, be it power, CFC or coherence [49].

This shows that neural oscillations can be a powerful tool. AD, PD, and schizophrenia patients benefit greatly from early diagnosis and treatment. In such cases, the non-invasive nature of EEG makes it especially valuable, possibly enabling detection of subtle changes in brain activity that may precede the onset of clinical symptoms. Understanding why these changes ocurr in the first place provides insights into underlying mechanisms, so that targeted therapeutic interventions can be developed.

### 1.4.1 Utility of Animal Models in Neuroscience

Much can be done with just scalp EEG, but at times it is necessary to pinpoint activity more closely (to get a look at a particular region, or a group of cells). Using an ECoG or implanting electrodes into the brain is, by nature, an invasive procedure that carries certain risks [50]. Most of intracranial neural recordings from human subjects come from epilepsy and PD patients, where undergoing such a procedure is necessary for treatment.

Implanting electrodes in healthy human subjects merely to study brain function is difficult to justify. For that reason, animal models are extremely useful. This does not eliminate the ethical problems [51], but it leaves some room for inquiry.

The mouse and the rat are the most popular animal model in neuroscience today [52]. Their brains share many fundamental features with human brains, including key neurotransmitter systems and neural circuitry. Additionally,

especially rats exhibit complex behaviors which can provide insights into higher cognitive functions such as learning, memory, emotion and social cognition. Despite that, some researchers propose, that a greater diversity of subject animals should be employed [52]. Through genetic manipulation, it is possible to derive animals that exhibit some traits of neurodegenerative or neuropsychiatric diseases and study them [53], [54], [55]. While certain therapies effective in animals may not directly translate to humans, the development of human treatments would simply not be possible without animal models in our world.

## 1.5 Local Field Potential (LFP) Signal Processing

Activity of neurons results in sources and sinks of cellular current. When these are separated by distance, dipoles form, resulting in field potentials which can be measured with an electrode inserted directly into the tissue. Despite the term "local", LFPs may not reflect local activity, since most of the activity comes from distant regions by volume conduction [56]. This signal is very similar to EEG and many EEG processing techniques can also be employed for LFPs. The most obvious difference EEG measures the summed activity of billions of neurons, with brain layers closest to the scalp electrodes having the greatest impact.

LFPs are recorded with electrodes inserted directly into the brain. Simplest electrodes are just thin metal wires with insulation on the surface, except for the tip. More sophisticated types exist and are frequently used, but metal-wire electrodes are still common, precisely because of their simplicity and also low cost.

### 1.5.1 Technical Limitations of LFP Recordings

Electrodes for recording LFPs have limited spatial resolution. Also, it is not possible to determine which neurons' activity gave rise to the recorded LFP without tracking the activity of all individual neurons in the brain.

Mammalian brains of common subject animals consist of billions of neurons and we can only record the activity of a small fraction. It has been estimated, that when recording LFPs, the signal originates from cells within 50-350$\mu$m radius with the electrode tip at its center. This is an oversimplification, but it makes for a simple example.

Let's consider a 250$\mu$m radius, which is commonly used [57] (in cat V1, but that will suffice here). The average neuronal density in the cerebral cortex of a mouse is $9.2 \times 10^4$ neurons/mm$^3$ [58]. Thus, the total activity of roughly 6000 neurons makes up the signal. Even considering the smallest radius of 50$\mu$m, that still leads to 50 neurons, which does not seem like much, but separating their activity, even with multi-channel silicon probes is a discipline with its own challenges.

Still, one electrode has a poor spatial resolution, in contrast to the excellent temporal resolution. Straightforward solution is to increase the number of

electrodes, but then there is also more signal to process. Doing so, getting reliable long-term recordings is still a challenge. Electrodes usually cause damage to the surrounding tissue, which gets worse over time, and the quality of the signal deteriorates. Recent progress in electrode design could see this problem resolved, should modern probes become widely accessible [59].

### 1.5.2 Difficulties of LFP Interpretation

Linking the exact purpose of neural oscillations in different behaviors is challenging, especially since animals exhibit a wide selection of them. Also, as mentioned previously, some rhythms arise and pass in a manner that is quite unintuitive. Certain rhythms correlate with overall decreased activity of neurons (alpha/beta in the cortex), but this likely does not hold for all brain areas.

It is known that neural activity gives rise to oscillations, but the underlying mechanisms as to how this happens for all of the rhythms are not. There are many types of neurons all with specific properties, and new ones are still being discovered. On top of that, only certain types of neurons can give rise to strong LFPs. Activity of those that contribute in only a minor way is hidden [56].

LFP is generated by current sources and sinks distributed in space. However, most of those currents cancel each other out, and what the electrode records is only a small fraction of total activity [56]. Volume conduction complicates things further, since without having multiple measuring sites, it is impossible to tell where the source of the LFP is, and it can result in misleading values of some metrics, such as coherence [60].

## 1.6 Motivation

Due to PAC being proposed as an important mechanism for the coordination of neural activity and information processing, which has been frequently reported in literature, I chose several methods for its detection. I employed methods which allow cross-frequency analysis on individual electrodes, though they may as well be used for the evaluation of PAC across electrodes [61]. Under the assumption, that both low and high frequency activity originate near the electrode, it is possible to examine PAC (or the rate of strong coupling events) in the area across experimental conditions. Here I have analyzed four pilot hippocampal recordings from an available dataset. The hippocampal theta rhythm has been linked to an array of behaviors and brain states [12]. Hippocampal theta-gamma coupling has also been investigated frequently and there are reports that even coupling of multiple theta and gamma frequencies can exist simultaneously, presumably for the communication of different groups of cells [62]. Since our dataset contains long recordings of background activity under urethane anesthesia, the main interest is on a preliminary exploratory analysis of the recordings at hand.

# Chapter 2

# Data and Methods

## 2.1 Simulated Data

I created surrogate data with events of PAC in order to get familiar with the methods employed. I have generated these in a very simplistic fashion. Such a signal will likely never be found in a real recording, but it works well enough to visually examine outputs of methods for coupling. For that I used the following equations:

$$W_{\text{slow}}(\mathbf{t}) = A_{\text{slow}} \cdot \sin(2\pi f_{\text{slow}}\mathbf{t}) \quad \text{... slow oscillation component} \quad (2.1)$$

$$W_{\text{fast}}(\mathbf{t}) = A_{\text{fast}} \cdot \sin(2\pi f_{\text{fast}}\mathbf{t}) \quad \text{... fast oscillation component} \quad (2.2)$$

$$M(\mathbf{t}) = \frac{1 + m \cdot \sin(2\pi f_{\text{slow}}\mathbf{t} - \phi)}{1 + m} \quad \text{... modulation factor} \quad (2.3)$$

$$W_{\text{modulated fast}}(\mathbf{t}) = W_{\text{fast}}(\mathbf{t}) \cdot M(\mathbf{t}) \quad \text{... modulated fast oscillation} \quad (2.4)$$

$$S(\mathbf{t}) = W_{\text{slow}}(\mathbf{t}) + W_{\text{modulated fast}}(\mathbf{t}) \quad \text{... signal with PAC} \quad (2.5)$$

where $\mathbf{t}$ is a time vector, $A_{\text{slow}}$, $f_{\text{slow}}$, $A_{\text{fast}}$, $f_{\text{fast}}$, are amplitudes and frequencies of the respective components, $m$ determines the modulation strength, and $\phi$ is the phase offset of the modulation factor to $W_{\text{slow}}(\mathbf{t})$.

By setting values of $m$ in range 0 and 1, it is possible to create $W_{\text{fast}}(\mathbf{t})$ going from no modulation all the way to a fully modulated fast oscillation. Amplitudes $A_{\text{fast}}$, $A_{\text{slow}}$were chosen so that they were in the same proportion as in real recordings. Noise $\eta$ was generated from a long segment of recorded signal by phase-shuffling, effectively destroying any consistent phase relationships. Now having both noise and signal components, energy can be calculated and then the signal is multiplied by a certain constant to fit a predefined signal-to-noise ratio (SNR). Afterwards, the signal and noise components were summed together. I am preserving the noise energy as it is from the shuffled recording and scaling down the energy of the generated signal, until a desired SNR is reached.

Here I am referring to SNR as:

$$SNR = \frac{E_S}{E_\eta},$$

where $E_S$ is the energy of signal with PAC and $E_\eta$ is the noise energy (calculated as sum of squares).

Setting SNR in this way may not be the best option, given that the energy of the noise is spread over many frequencies, while energy of the signal is concentrated in two frequencies. Another approach would be to add a more narrowband noise for each frequency component and gradually increase that, until energy of the noise surpasses one of the signal frequencies. I find noise generated by phase-shuffling real recordings a preferable approach, because it's closest to the kind of noise one can expect in real recordings. Also, for visual comparison of results on simulated data, the exact SNR value is not so important, compared to showing how these methods behave under increasing levels of noise.

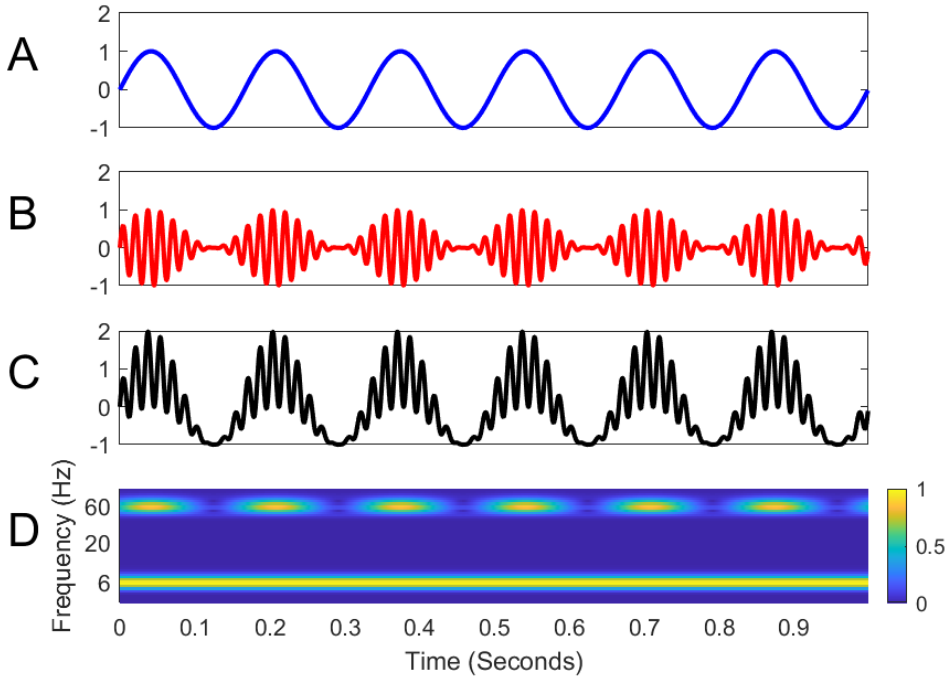


**Figure 2.1:** Example of signals generated by Equations 2.1, 2.4, 2.5. For clarity, both amplitudes were set to 1 with a phase offset of 0 and $m = 1$. (A) Low frequency component (6Hz). (B) High frequency component (60Hz) modulated by low frequency component. (C) Sum of A and B. (D) Magnitude scalogram of signal from C.

Signals for analysis consist of 11 segments of coupling events (such as the one in 2.1) with gradually increasing modulation from $m$ = 0,0.1,0.2,...1, starting from no amplitude modulation all the way to a fully modulated fast wave. I set slower oscillation at 6Hz and the faster at 60Hz, roughly choosing

the middle of theta and gamma range with a phase offset of $\phi = \frac{\pi}{2}$. The phase offset could have been set to a random number, since methods used do not rely on it. They are however capable of detecting this phase offset. Each coupling event lasts 20 cycles of the slower oscillation, (so about 3.3 seconds), with 80 cycles (13.3 seconds) of space or noise in between. This spacing ensures that even with relatively long time window settings for some methods, individual segments won't blend into each other, which could artificially inflate the coupling estimate.

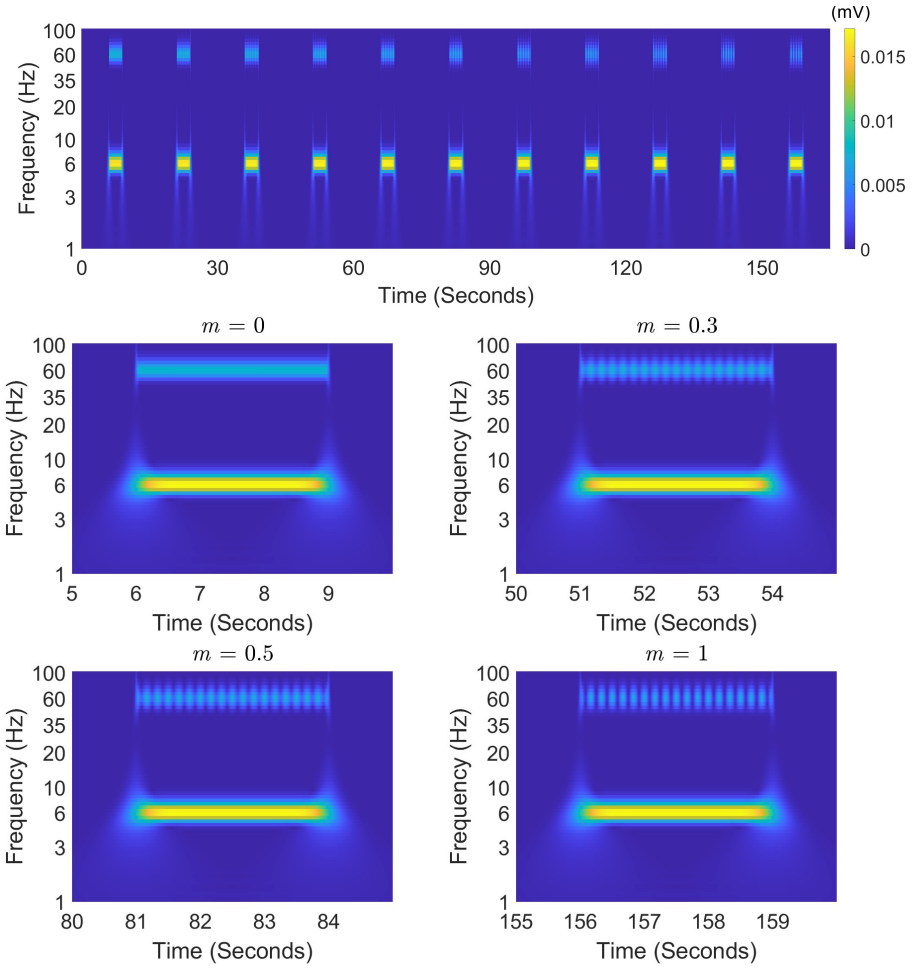


**Figure 2.2:** Time-frequency representation of simulated signal with segments of PAC (without noise). Top shows the magnitude scalogram of the whole signal. Lower plots show zoomed-in portions thereof with PAC events for different values of $m$. When $m = 0$, there is no modulation, hence uninterrupted line appears at 60Hz. As $m$ increases, the 60Hz amplitude gets smaller around certain phase values of the 6Hz component (here $\frac{\pi}{2}$). When $m$ reaches 1, the 60Hz amplitude is modulated all the way to zero. Since each coupling event in the chain lasts 20 cycles of 6Hz component (3.3 seconds), the scalogram should show 20 stripes at 60Hz. Edge effects add two extra at the beginning and end, since segments were not windowed. I have chosen to ignore them, since these artifacts were more predictable than those caused by windowing. They also get lost after adding noise.

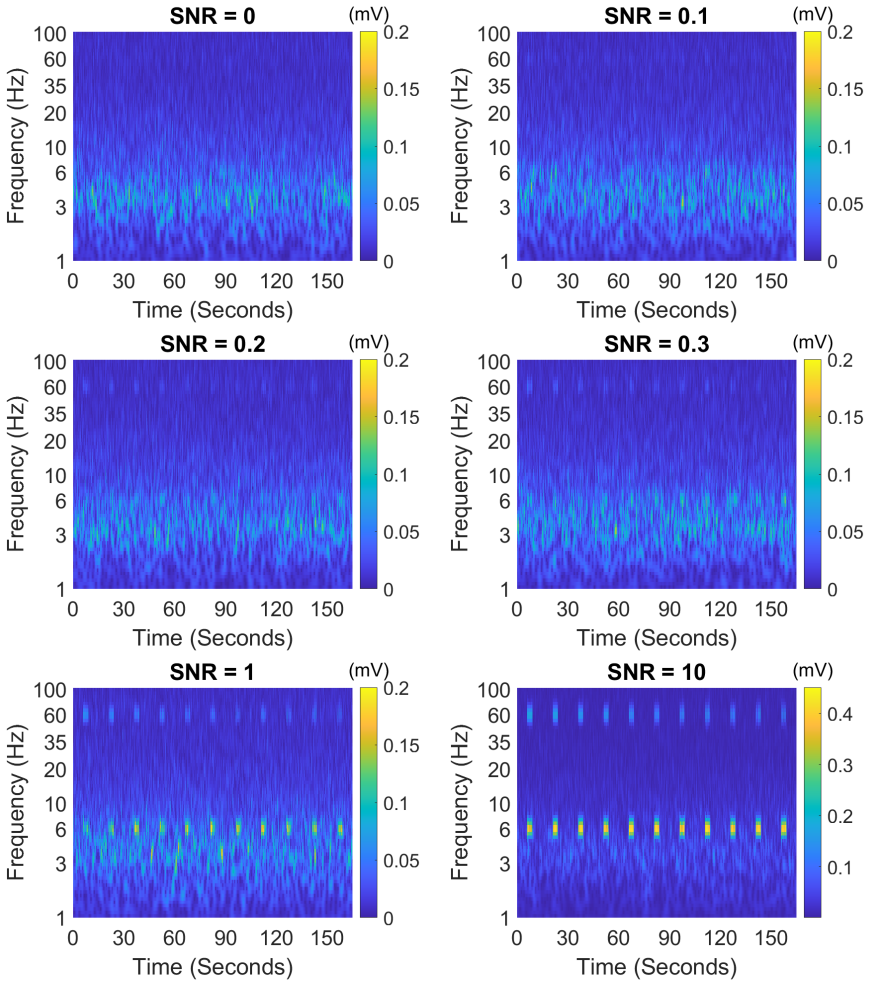


**Figure 2.3:** Magnitude scalograms of signals with coupling event after adding increasing amounts of noise. Top left signal consists purely of noise. Energy of coupling events in the bottom right are ten times greater than energy of noise. The edge effects seen in Figure 2.2 are overshadowed by noise in most cases. Note how the 60Hz component is more difficult to see with increasing $m$.

When timestamps with events of interest are available alongside recordings, it is possible to construct commodulograms and examine which slower frequencies are coupled to fast frequencies. Another approach is to pick a slow frequency (or a range of slow frequencies) and calculate the coupling estimates for all higher frequencies and plot them in time, which is still very time-consuming. Approach later used for analysis of real recordings, was to pick one row of the wavelet coefficients corresponding to 60Hz and estimate the coupling for lower frequencies of 4-8Hz, with 1Hz steps. The wavelet with 60Hz center frequency should be broad enough in the frequency domain to capture possible coupling in about 50-70Hz.

## 2.2 Animals and Surgeries

Four PV-cre transgenic mice (B6.129P2-Pvalbtm1(cre)Arbr/J; n = 2 males + 2 females, age 12 weeks) were used to determine the effect of brain-wide activation of PV interneurons on neuronal activity. The PV-Cre mice were transduced with the DREADD viral vector AAV2-hSyn-DIO-hM3(Gq)-mCherry (#50474-AAV2, Addgene) and implanted with electrodes for electrophysiological recordings four weeks prior to experiments. All surgical manipulations were performed under 2-4% isoflurane anesthesia. Injections of the viral vector (at a concentration of $4 \times 10^{10}$ gc/mouse) were administered into the left jugular vein through the pectoral muscle. Recording electrodes (250$\mu$m silver wire with insulation, A-M Systems) were implanted bilaterally during the viral transduction surgery chronically into the dorsal hippocampus (dHPC; AP = -1.8, ML = ±1.2, DV = -1.5) and medial prefrontal cortex (mPFC; AP = 2.4, ML = ±0.5, DV = -1.2) measured from the bregma, with coordinates selected according to Paxinos and Franklin [63]. Using dental acrylic, two anchoring screws were used to attach the implant firmly to the skull. One additional anchoring screw, placed above the cerebellum, served as a ground and reference electrode for the recording electrodes. After surgery, animals had free access to drinking water with antibiotics, analgesics, and anti-inflammatory drugs for five days. Mice were housed in pairs in a temperature-controlled room (21°C) with a 12-h light-dark cycle for a recovery period of four weeks before experiments. All animal experiments complied with a protocol approved by the IPHYS ethical committee for animal welfare and current legislation (the Animal Protection Code of the Czech Republic and EU Directive 2010/63/EC).

| **Female** | **Male** |
|---|---|
| f477 | m135 |
| f478 | m484 |

**Table 2.1:** Identification codes of animals used to refer to them throughout work.

## 2.3 LFP Recordings in Anesthetized Mice

Mice were anesthetized with urethane (1.5 g/kg; i.p.) injected in two half-doses (0.75 g/kg each) given 10 minutes apart. Additional doses of urethane (0.15 g/kg) were administered if necessary. LFP activity was recorded bilaterally from the dHPC and mPFC. Anesthetized mice were injected with saline (1 ml/100g body weight; i.p.) and a 50-min recording was conducted (saline recording). Subsequently, mice were injected with C21 (Hellobio, cat #HB4888), specific DREADD agonist (1 mg/kg dissolved in 1 ml/100g body weight of saline; i.p.), and recorded for another 50-min period (C21 recording). Neural data from all recording channels were amplified (1000x), and the raw signal was limited by anti-aliasing band-pass filter at 1-475Hz and sampled at

$f_s = 2$kHz with Micro 1401-3 Data Acquisition Unit (Cambridge Electronic Design, UK).

I selected the last 10 minutes of saline and C21 recordings for analysis, since after 40 minutes the receptors should be strongly activated by the injected compound. Then I've filtered each recording with an IIR comb filter (using `iircomb` function) with notches at 50Hz multiples to get rid of powerline noise. To decrease phase distortion, I used the `filtfilt` function, which performs zero-phase filtering. Each signal was wavelet transformed to get wavelet coefficients (and from that phase and amplitude information) for 1-100Hz components. Upper limit of 100Hz was chosen per the limitations of the recording system and lower data quality above 100Hz. Methods for PAC estimates were set up to detect theta-gamma PAC (theta: 4-8Hz, gamma: 50-70Hz).

## 2.4 Discrete Hilbert Transform (DHT)

The Hilbert transform is a mathematical operation that can be applied to a real-valued signal to obtain an analytic signal. This analytic signal is a complex-valued function that captures both the amplitude and phase information of the original real-valued signal.

For discrete signals, the process begins by computing the Fast Fourier transform (FFT) of the input discrete signal, decomposing it into its frequency components. In the frequency domain, the FFT produces a complex-valued spectrum with positive and negative frequency components. To obtain the analytic signal, the negative frequency components are typically discarded by setting them to zero. Signal is then reconstructed via inverse FFT, ending up with the analytic signal in the time domain. The DHT can be formally written as:

$$\hat{s}[k] = DHT\{s[n]\} = \begin{cases} \frac{2}{\pi} \sum_n, \frac{s[n]}{k-n}, & \text{if } k \text{ is even}, n \text{ is odd} \\ \frac{2}{\pi} \sum_n, \frac{s[n]}{k-n}, & \text{if } k \text{ is odd}, n \text{ is even} \end{cases} \tag{2.6}$$

where $n$ ranges over the samples of the original signal and $k$ ranges over the samples of the transformed signal $\hat{s}[k]$.

From this, the instantaneous amplitude $A[n]$ and phase $\phi[n]$ of the signal can be extracted:

$$A[n] = |\hat{s}| \tag{2.7}$$

$$\phi[n] = \arg(\hat{s}) \tag{2.8}$$

MATLAB allows all of these operations very conveniently within the functions `hilbert, abs, angle` [64]. It should be noted, that for extracting meaningful phase values after DHT, relatively narrowband signal is required.

## 2.5 Continuous Wavelet Transform (CWT)

CWT is a powerful tool for time-frequency analysis. It decomposes a signal into its constituent frequency components by convolution with a series of wavelets with varying frequencies and scales, providing a detailed representation of its frequency content as it evolves over time. The CWT is defined as:

$$CWT_x(a,b) = \frac{1}{\sqrt{|a|}} \int_{-\infty}^{\infty} x(t)\psi^* \left(\frac{t-b}{a}\right) dt, \tag{2.9}$$

where $x(t)$ is the input signal, $a$ is the scale parameter, $b$ is the translation parameter, and $\psi^*(t)$ is the complex conjugate of the analyzing wavelet function.

I've opted for, Morse wavelets [65], but the choice likely isn't critical. Fourier transform of Morse wavelet is:

$$\psi_{P,\gamma}(\omega) = U(\omega)\, a_{P,\gamma}\, \omega^{\frac{P^2}{\gamma}}\, e^{-\frac{\omega}{\gamma}}, \tag{2.10}$$

where $U(\omega)$ is the unit step function, $a_{P,\gamma}$ is a normalizing constant, $P$ is the time-bandwidth product, and $\gamma$ characterizes the symmetry of the Morse wavelet.

All instances CWT were obtained with MATLABs `cwt` in conjunction with `cwtfilterbank` to speed up the calculations, since one needs to obtain the wavelet filterbank only once at the start [66], [67]. The settings for `cwtfilterbank` in all cases were: `VoicesPerOctave=10, FrequencyLimits=[1 100]`. Other parameters were left at default, meaning $\gamma = 3, P^2 = 60$.

Wavelet coefficients obtained in this way carry both the amplitude and phase information which can be extracted in the same manner as with DHT. The real part of each row of these coefficients essentially contains the original signal, which was bandpass filtered by the corresponding wavelet. Using this filterbank has a drawback, since wavelets with high center frequencies tend to be quite broad in frequency domain, so there there is no clear cutoff frequency. On the upside, designing a wavelet filterbank this way is rather simple compared to creating a traditional FIR bandpass filterbank.

## 2.6 Mean Vector Length Modulation Index (MVL MI)

This method was originally introduced by Canolty et al. [68], and subsequently Özkurt et al. proposed a normalization factor for MVL MI which accounts for variations in amplitude time-series of the high frequency component [69].

Here are the steps to obtain MVL MI with amplitude normalization factor: 1: Select a segment of recording. 2: Extract phase time-series of the slow oscillation and amplitude time-series of the fast oscillation (either by

performing DHT on bandpass filtered signal components, or as in this work, by CWT, results should be comparable). 3: Get a result from the equation:

$$MVL\ MI = \frac{1}{\sqrt{N}} \frac{\left| \frac{1}{N} \sum_{n=1}^{N} \mathrm{a}_f(n) e^{i(\phi_s(n))} \right|}{\sqrt{\frac{1}{N} \sum_{n=1}^{N} \mathrm{a}_f(n)^2}}, \tag{2.11}$$

where $\mathrm{a}_f$ is the amplitude time-series of the fast oscillation, $\phi_s$ is the phase time-series of the slow oscillation, $N$ is the number of samples in the signal segment and $n$ is the n-th sample point.

I chose 2000ms time windows for the analysis of LFP recordings with 200ms steps. I have done the same for surrogate data, while also trying out 500ms time windows with 10ms steps. The choice was made according to previous work of Seymour et al., who've noted that modulation indices return inflated coupling values for time windows shorter than 1 second [70]. The 500ms is for comparison with the longer window choice.

Instead of taking the absolute value of the numerator from Equation 2.11, it's also possible to extract phase value of the complex vector. Further details can be found within the supplementary work of [68].

## 2.7 Phase-Locking Value Modulation Index (PLV MI)

This modulation index by Cohen shares some similarities with the MVL MI. First two steps of calculations are the same (i.e. choose a segment and extract phase and amplitude time-series of slow and fast oscillation), but then the amplitude time-series is Hilbert transformed to obtain the phase time-series of the envelope. Cohen notes, that it is required to normalize, de-trend or subtract the mean from the envelope before the transform to avoid throttling the phase values. For simplicity, I chose to remove the mean of each analyzed segment. In contrast to the MVL MI, this method does not consider the amplitude values of the high frequency components at all.

$$PLV\ MI = \left| \frac{1}{N} \sum_{n=1}^{N} e^{i(\phi_s(n) - \phi_{\mathrm{a}_f}(n))} \right|, \tag{2.12}$$

where $\phi_s$ is the phase time-series of the slow oscillation, $\phi_{\mathrm{a}_f}$ is the phase time-series of the envelope of fast frequency oscillation. $N$ and $n$ is the same as in Equation 2.11.

I chose equal time windows as in the case of MVL MI for comparison between methods. Again, the PLV MI is the absolute value of the complex vector in Equation 2.12, but it's possible to obtain phase information as well with `angle`.

## 2.8 Magnitude Squared Wavelet Coherence

Wavelet coherence provides a localized measure of correlation in both time and frequency domains. I am using MATLABs implementation `wcoherence` for all calculations [71]. It is mathematically defined by:

$$W_{\text{Coh}}(a,b) = \frac{\left|S_m(C_x(a,b)C_y^*(a,b))\right|^2}{S_m(|C_x(a,b)|^2) \cdot S_m(|C_y(a,b)|^2)}, \tag{2.13}$$

where $C_x(a,b), C_y(a,b)$ are wavelet coefficients of the input signals $x$ and $y$ at scales $a$ and times $b$, $S_m$ is the smoothing function (in MATLABs case a moving average window) and $*$ is the complex conjugate operator.

The term inside the smoothing function in the numerator of Equation 2.13 is the (unsmoothed) wavelet cross-spectrum:

$$W_{\text{Cross}}(a,b) = C_x(a,b)C_y^*(a,b), \tag{2.14}$$

The denominator of Equation 2.13 is the normalization factor which ensures that magnitude-squared wavelet coherence returns results in range [0,1]. Wavelet coherence is typically used across electrodes, but by calculating the wavelet coherence of the slow frequency components (4-8Hz) and the envelope of the fast time-series a measure of PAC can be obtained. Should these two signals have a consistent phase relationship, they will have high coherence. In this manner it is similar to the PLV MI.

## 2.9 Cliff's Delta

Cliff's Delta, also known as Cliff's $\delta$ (`meanEffectSize` function [72]), is a non-parametric effect size measure used to quantify the difference between two groups of data [73]. This effect size is suitable to use with Wilcoxon rank sum test, which I've used to determine the significance of changes across experimental conditions in LFP recordings (`ranksum` function [74]). The formula for Cliff's $\delta$ is given by:

$$\delta = \frac{2}{mn} \sum_{i=1}^{m} \sum_{j=1}^{n} \left(\text{sign}(X_i - Y_j)\right), \tag{2.15}$$

where $X = \{X_1, X_2, \ldots, X_m\}$ and $Y = \{Y_1, Y_2, \ldots, Y_n\}$ are the two groups being compared, $m$ and $n$ are the sample sizes of groups $X$ and $Y$ respectively.

Cliff's $\delta$ ranges from -1 to 1, and the magnitude can be generally interpreted as follows: small effect ($|\delta| < 0.147$), medium effect ($0.147 \leq |\delta| < 0.33$), and large effect ($|\delta| \geq 0.33$).

# Chapter 3

# Results

## 3.1 Simulated Coupling Data

First I tested outputs of MIs on simulated signals by choosing one lower frequency from which to extract phase values (6Hz) and calculating MIs for all higher frequencies (Figures 3.1, 3.2). The further the low and high frequencies are apart, the easier it is to detect PAC. In this case the $f_{\text{fast}} = 10 f_{\text{slow}}$. I haven't been able to detect coupling with much certainty for $f_{\text{fast}} < 5 f_{\text{slow}}$. Components with center frequencies of 50-70Hz show increased coupling estimates (almost 50-90Hz for high SNR). This is expected, due to how wide these wavelets are in the frequency domain.

How specific these methods are for the chosen lower frequency again depends on the frequency domain width of the filter that was used to obtain it. Thankfully, wavelets with low center frequencies are quite narrow in the frequency domain. Figures 3.3, 3.4 illustrate this for MIs and wavelet coherence/cross-spectrum. I have been unsuccessful with getting good frequency resolution from wavelet coherence between 4-8Hz components and envelope of the 60 Hz component with low SNR. Even for cases where very little noise was added, it seems to show high values across a range low frequencies (4-10Hz). Nevertheless, it at least lines up with the actual coupling events. The (unsmoothed) wavelet cross-spectrum on the other hand gives visually closer results to the MIs, which show high values mostly around 6±1Hz, clearly evaluating the 6Hz to 60Hz coupling. That said, neither wavelet coherence/cross-spectrum or the MIs are able to reliably pick up on segments where the coupling is weak (small values of $m$ from Equation 2.3).

## 3.2 Analysis of LFP Recordings

Due to achieving poor results with wavelet coherence on simulated data as well as computational complexity, I opted to use only MVL MI and PLV MI for the analysis of recorded LFPs. Both methods were set up with a time window of 2000ms and time steps of 200ms and in the same manner as for the simulated data in Figure 3.3. First and last 10 seconds were discarded due to edge effects, but their impact would likely be minor, given the whole

signal is 10 minutes long. Figure 3.5 shows an example output on real data. Having calculated these values, I used them to make the plots from Figure 3.5 more readable in hopes of identifying interesting areas in the 10 minute long recordings. This was done by getting the median (or 75th percentile) of each row in Figure 3.5 (from the saline recording only) and thresholding. All coupling estimates which fell beneath the selected threshold were set to zero. Results of this are in Figures 3.6, 3.7, 3.8, 3.9, for two different animals. Brief periods of increased coupling are visible with more clarity. These plots look mostly irregular, but sometimes, strong coupling occurs at a similar time in both hemispheres, see Figure 3.9.

All coupling estimates (rows in Figure 3.5) were averaged in 2000ms non-overlapping windows. I now had two vectors, one for saline and another for C21 recording containing time-averaged coupling estimates for all animals in both hippocampi. Figure 3.10 shows the medians of the two vectors for each lower frequency. As can be seen, coupling estimates are correlated across frequencies. For this reason, Cohen recommends averaging in time-frequency windows [61]. Hereafter, all coupling estimates were also averaged in the 4-8Hz range.

Under the assumption that the coupling estimates come from the same distribution in the left and right hippocampus, I joined the time-frequency averaged values into one vector (for saline and C21 recordings respectively), in order to examine overall changes in hippocampal theta-gamma PAC within subjects. I utilized Wilcoxon rank sum test. MVL MI values were significantly different for saline/C21 recordings ($p < 0.05$) in three animals with small to medium effect sizes, but the change was not consistent across animals. Animals f477 and m484 expressed increased theta-gamma PAC during C21 recording. The opposite was true for f478. Results are shown in Figure 3.11. For PLV MI the change was significant in all animals ($p < 0.05$), with medium to large effect sizes, but again the direction of change is not always the same. Results can be seen in Figure 3.12. Possible reasons for these shifts will be covered in Chapter 4.

Similarly to how I have combined PAC estimates from both hippocampi, I've also tried doing the same for all animals, thus getting vectors for saline/C21 recordings. Differences in MVL MI values were not significant. While PLV MI values were significantly different ($p < 0.05$), the effect size was small ($\delta = 0.12$). With a larger number of subjects, the males and females should be compared separately, but for the purposes of the preliminary analysis, I merged all animals into one group.

Lastly, I visually investigated whether there is any phase offset preference by constructing phase-amplitude plots from the MI values (Figures 3.13, 3.14). Again, mice f477 shows the most notable differences after the application of C21. Gamma is most strongly modulated at $\frac{3\pi}{2}$, or 0 and $2\pi$ of the theta phase. The $\frac{3\pi}{2}$ corresponds to the trough of theta. The deviations are strongest for 4-5Hz lower frequencies and look mostly uniform for 6-8Hz frequencies.

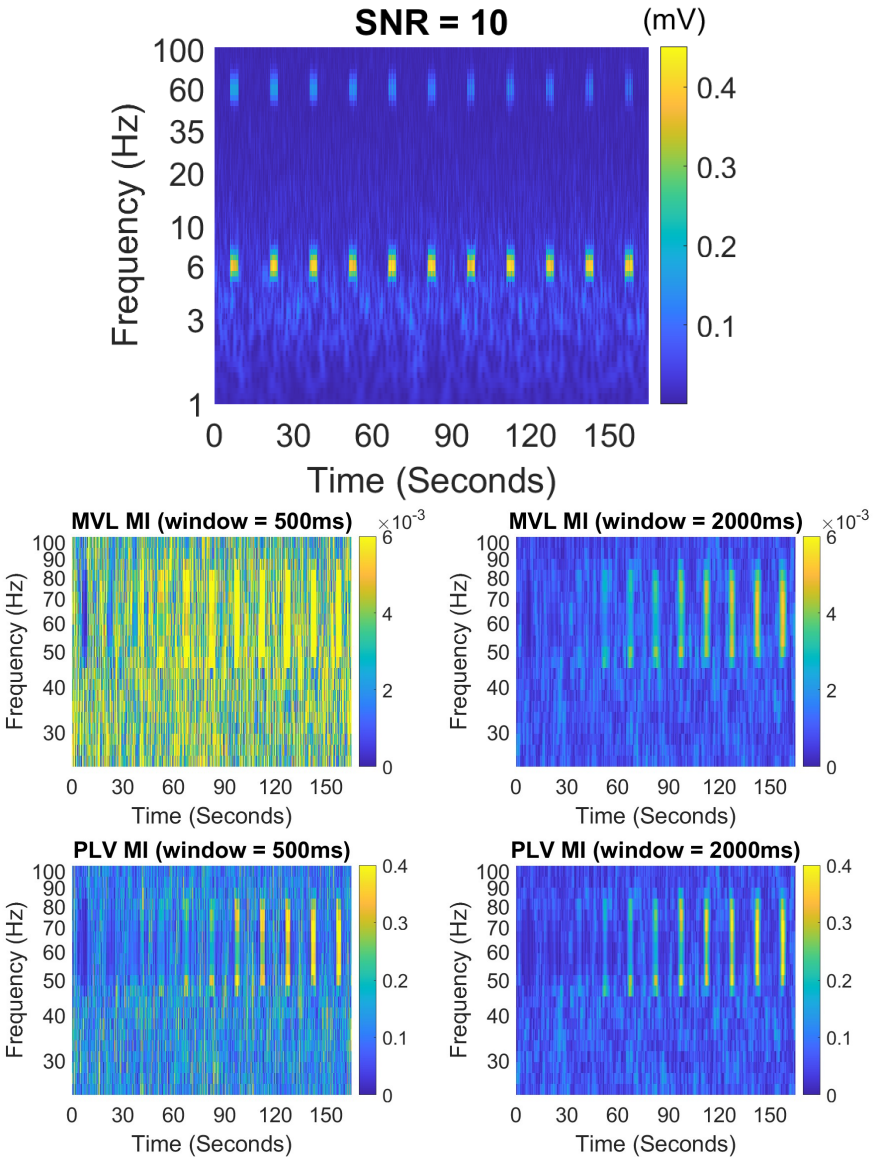


**Figure 3.1:** MI values calculated by extracting phase of 6Hz and envelopes or phases of envelopes of all higher frequencies (four lowest plots). Top shows magnitude scalogram of the input signal with added noise. Since the energy of the signal is high in this example, wavelets with center frequencies as far as 50-90Hz capture the modulation of 60Hz component. This gets better by adding more noise. Choosing short time windows results in inflated values of MIs in places where no coupling is present. The 500ms and 2000ms corresponds to 3 resp. 12 cycles of the 6Hz oscillation.

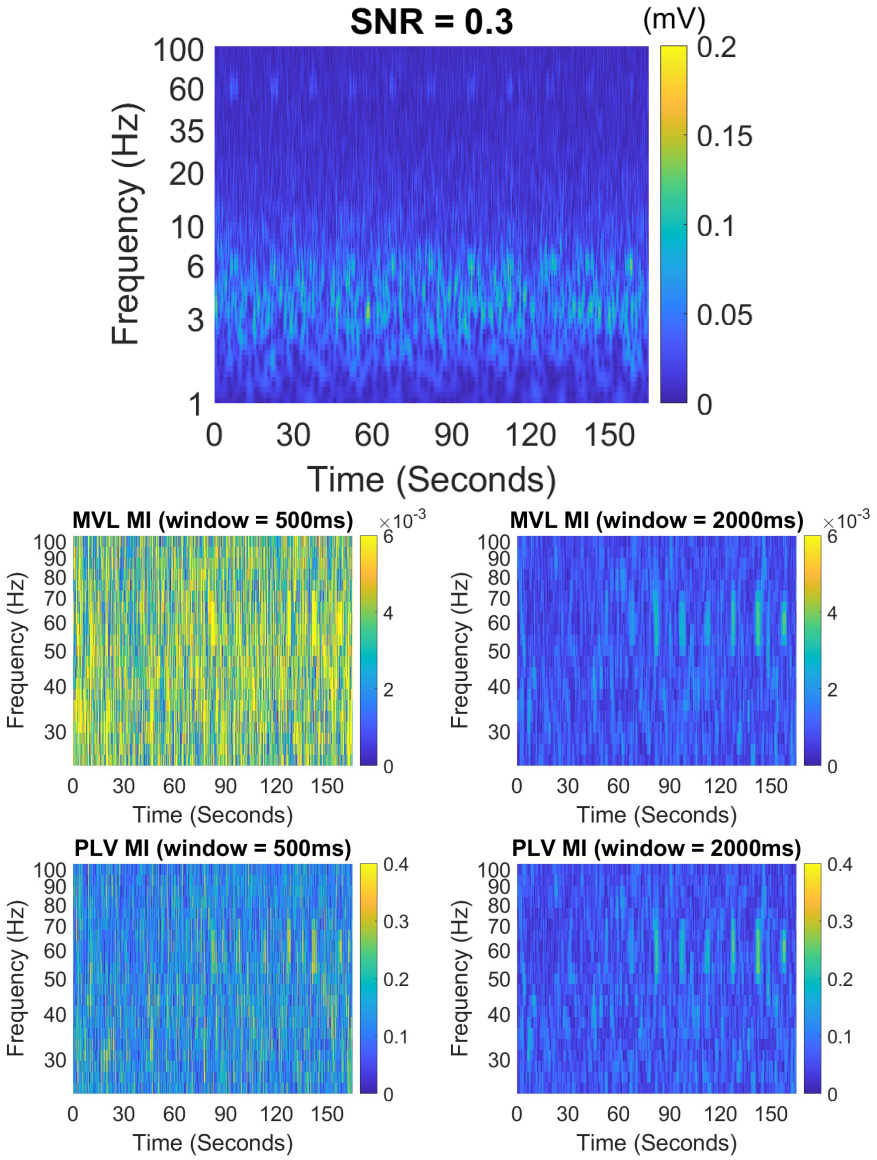


**Figure 3.2:** Same as Figure 3.1 for lower SNR. With more noise added, the spread along the frequency axis is now no more than 50-70Hz. In a way, even PLV MI is able to capture the strength of modulation, despite not considering amplitude values at all. That said, neither method really captures the coupling when amplitude modulation is weak, since the envelope/envelope-phase time-series gets overpowered by noise.

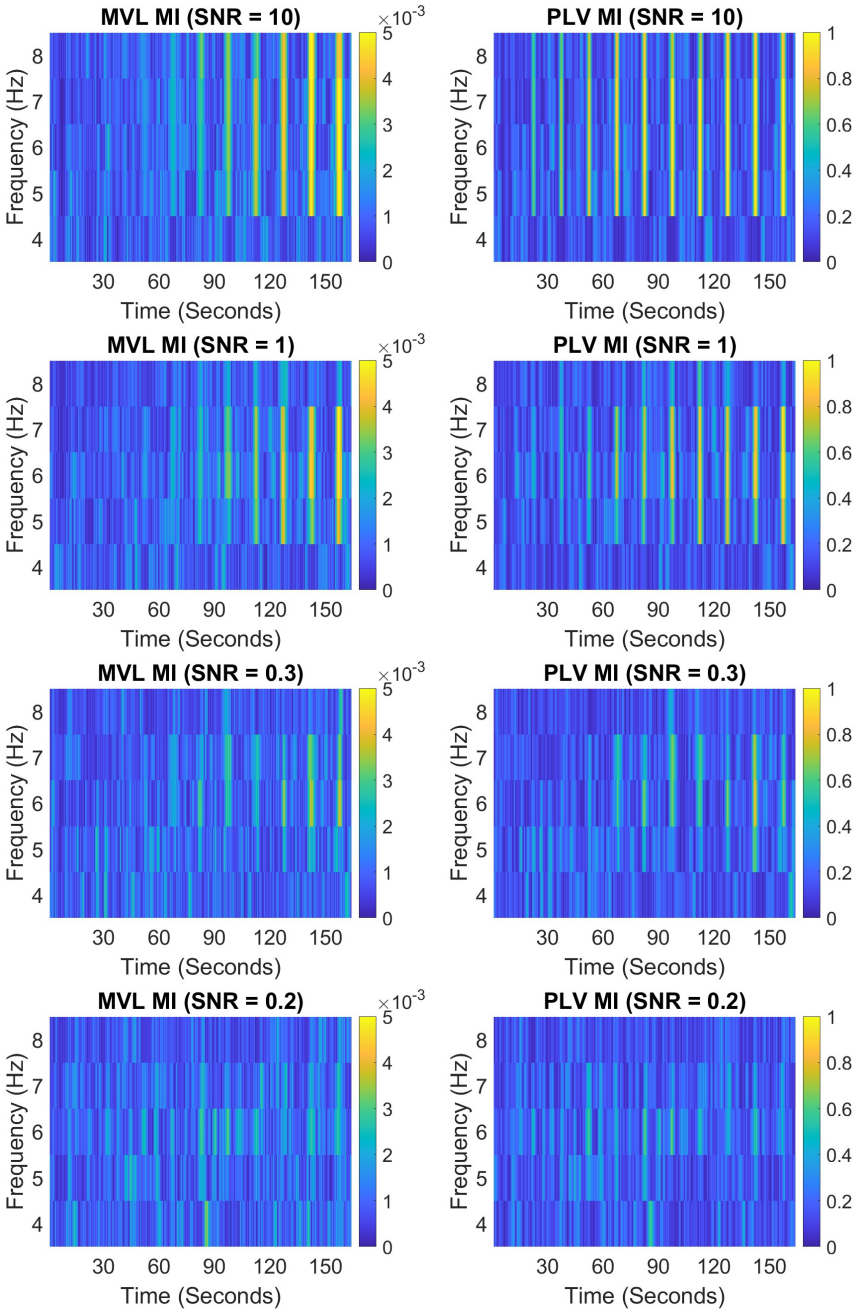


**Figure 3.3:** MI coupling values of 4-8Hz components (frequency axis) to 60Hz for different SNRs. MIs were calculated with 2000ms time windows and 200ms steps. As SNR decreases, the MIs show increased values for 6±1Hz. For SNR $< 0.3$, regions with and without coupling look much the same.

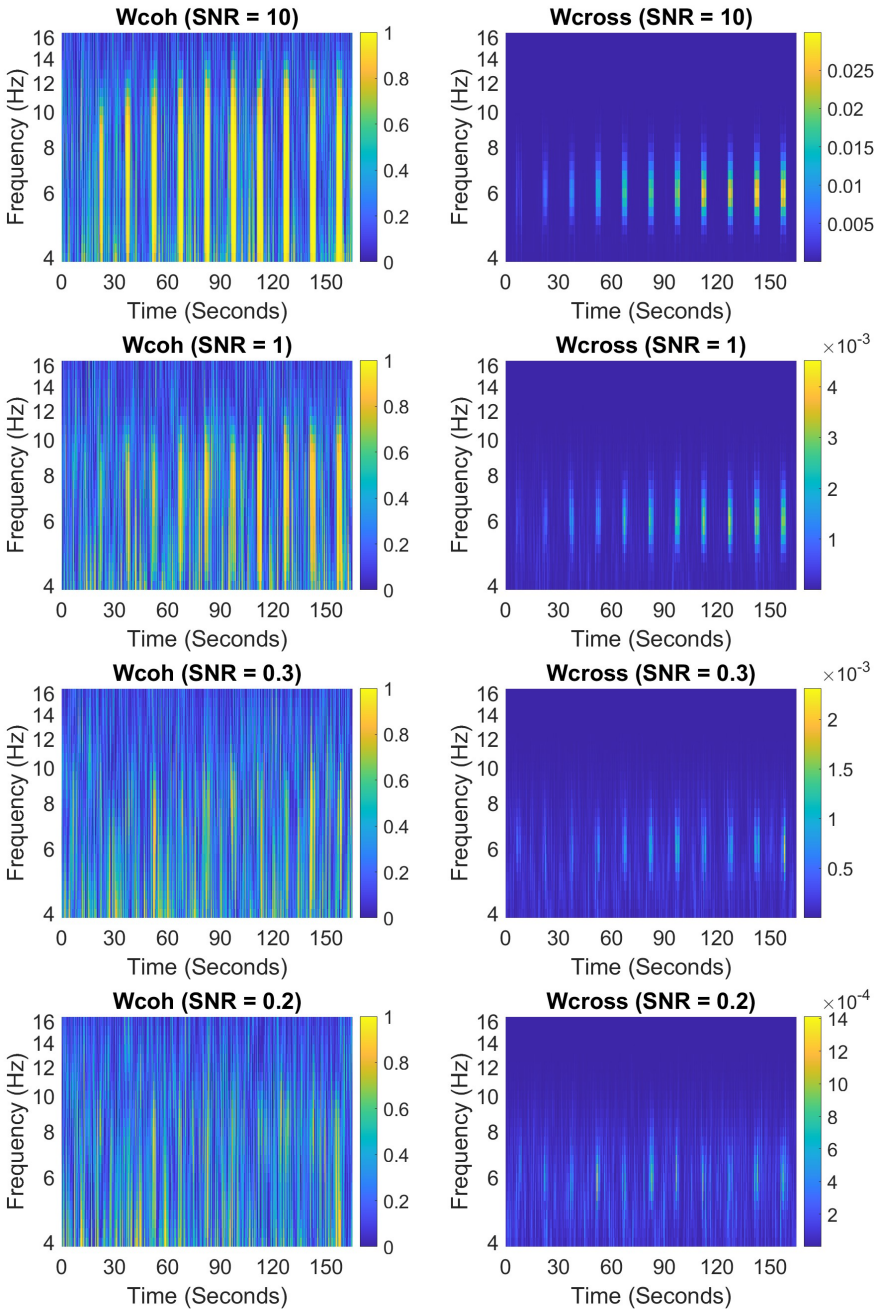


**Figure 3.4:** Comparison of wavelet coherence and magnitude of wavelet cross-spectrum for different SNRs. Input signals are 4-8Hz components and envelope of the 60Hz component (similar to Figure 3.3). The cross-spectrum shows better frequency resolution, but isn't normalized (varying ranges of colorbars).

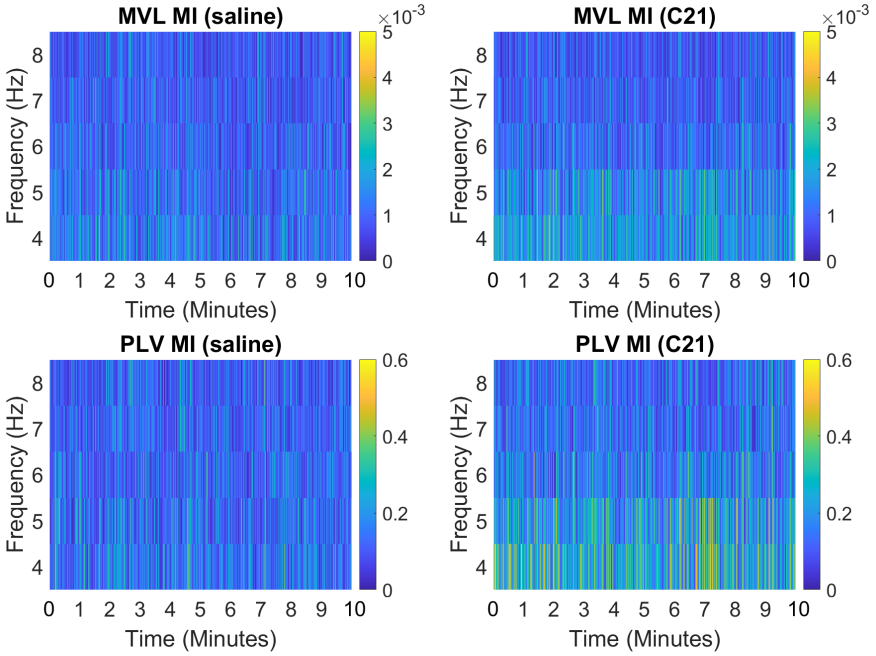


**Figure 3.5:** Results from right hippocampal recordings of animal f477 which presents greatest difference between coupling estimates during respective 10 minute segments. This figure is mainly for illustration. Other animals do not exhibit such stark contrast between saline/C21 or, in this case, also across hemispheres. As expected, there will hardly ever be regions of coupling that last 20 cycles (as in the surrogate data), and no such clear regions of high coupling values for 6-8Hz are visible here.

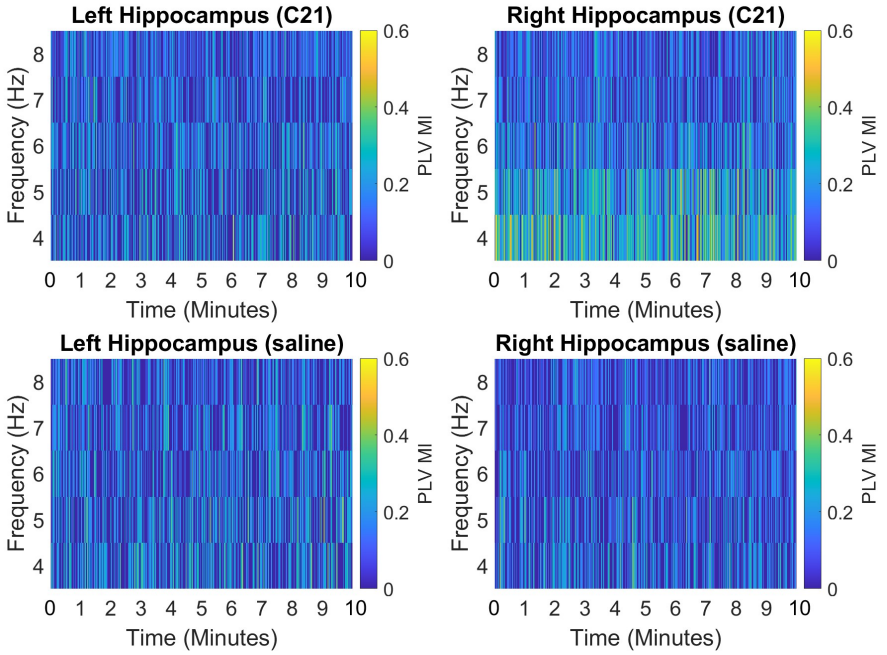


**Figure 3.6:** Median-thresholded PLV MI values from animal f477. Displaying results for both hemispheres (on the left resp. right) and experimental conditions (top: C21, bottom: saline).

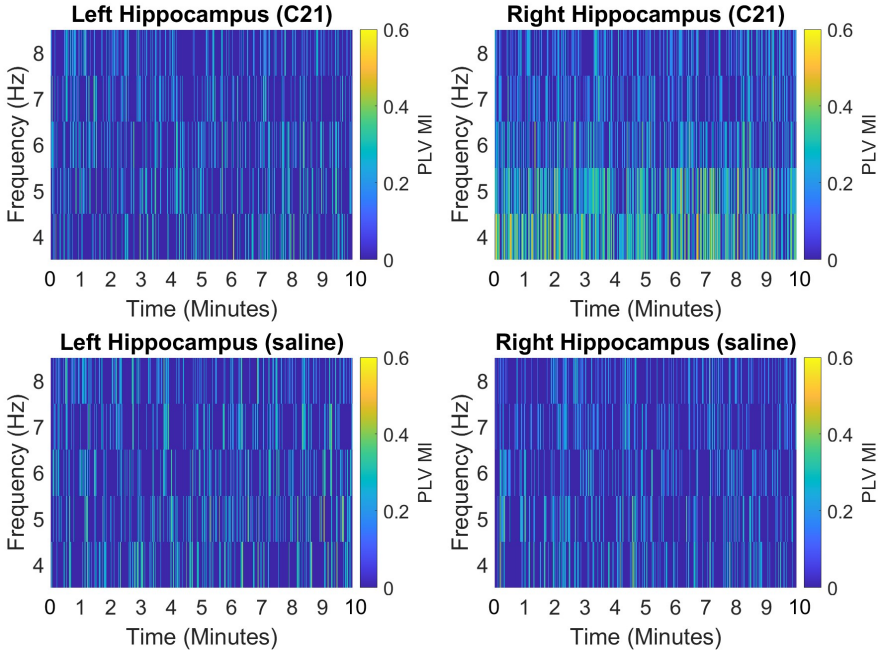


**Figure 3.7:** 75th percentile-thresholded PLV MI values from animal f477. Displaying results for both hemispheres (on the left resp. right) and experimental conditions (top: C21, bottom: saline).

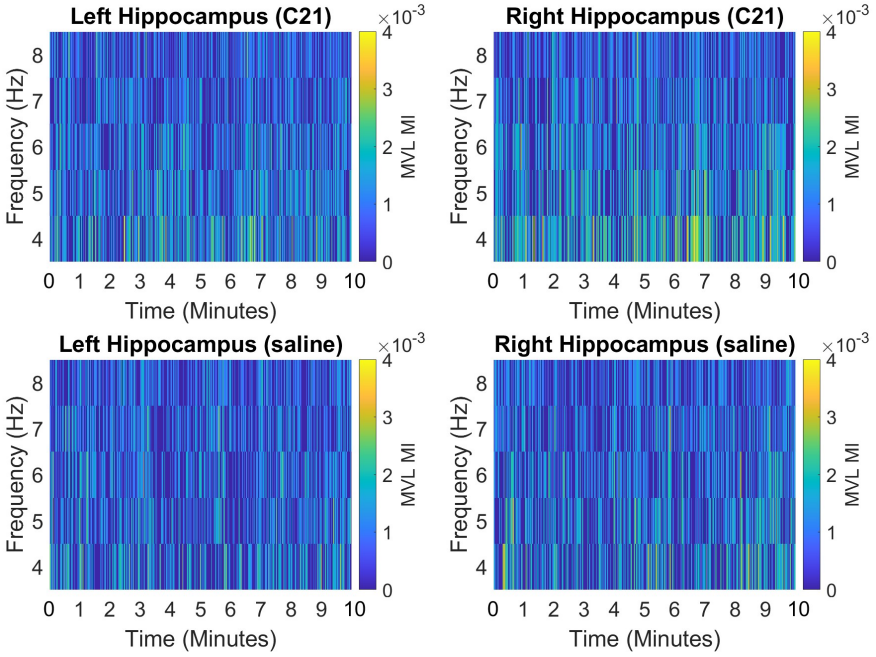


**Figure 3.8:** Median-thresholded PLV MI values from animal m484. Displaying results for both hemispheres (on the left resp. right) and experimental conditions (top: C21, bottom: saline).

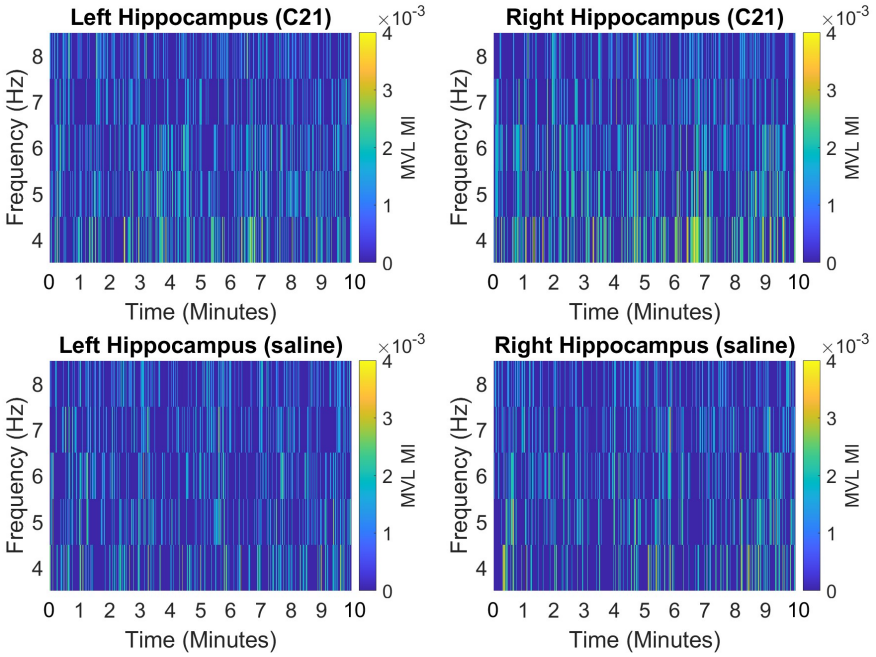


**Figure 3.9:** 75th percentile-thresholded MVL MI values from animal m484. Displaying results for both hemispheres (on the left resp. right) and experimental conditions (top: C21, bottom: saline). Note the high MVL MI values for C21 recordings in both hemispheres around the 7 minute mark.

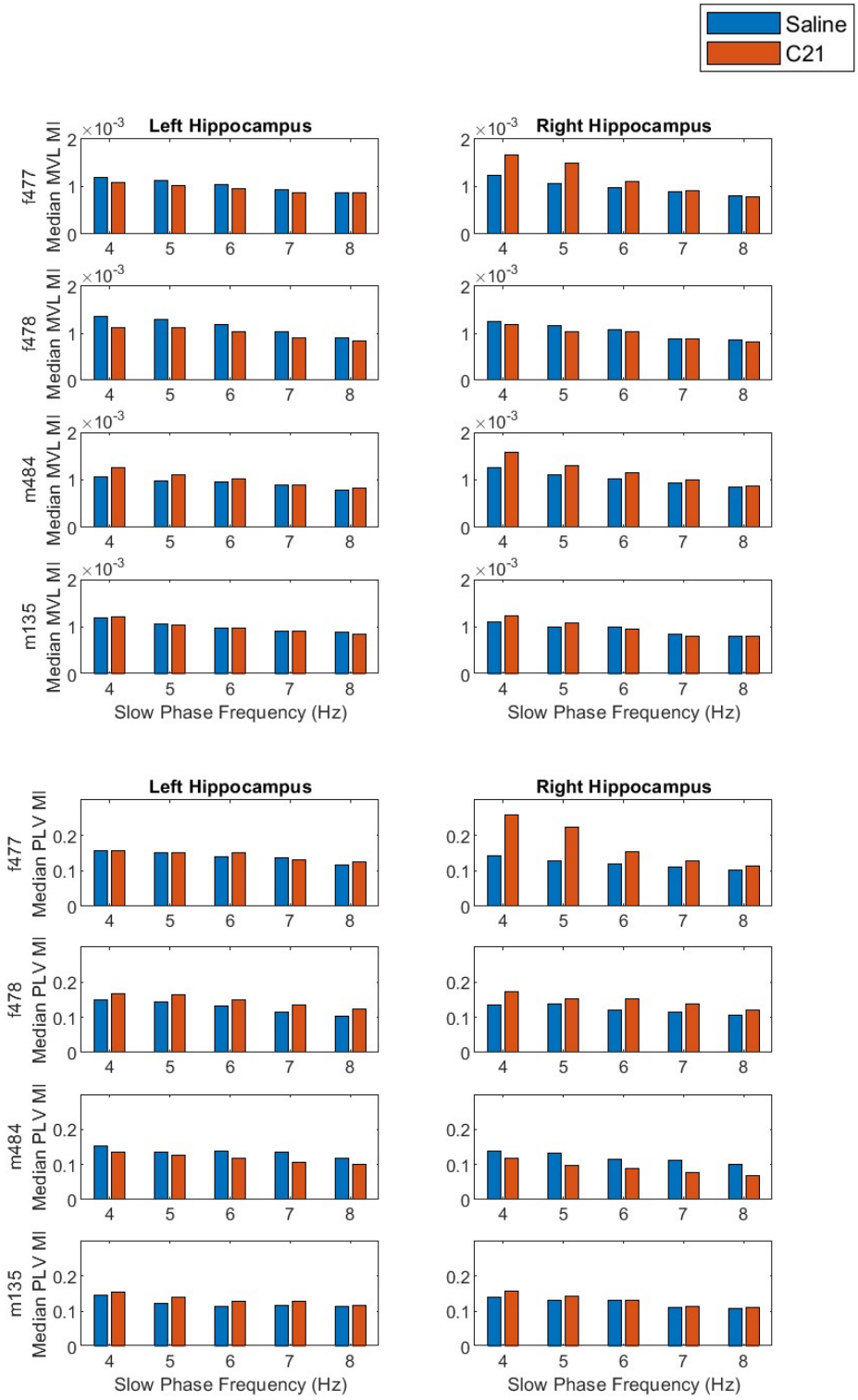


**Figure 3.10:** Median values of time-averaged coupling estimates over 10 minute recording for both experimental conditions. Results shown for each method, animal, hippocampus and low frequency separately. Note the correlation of coupling estimates for adjacent frequencies. This illustrates the necessity of also averaging across the frequency range.

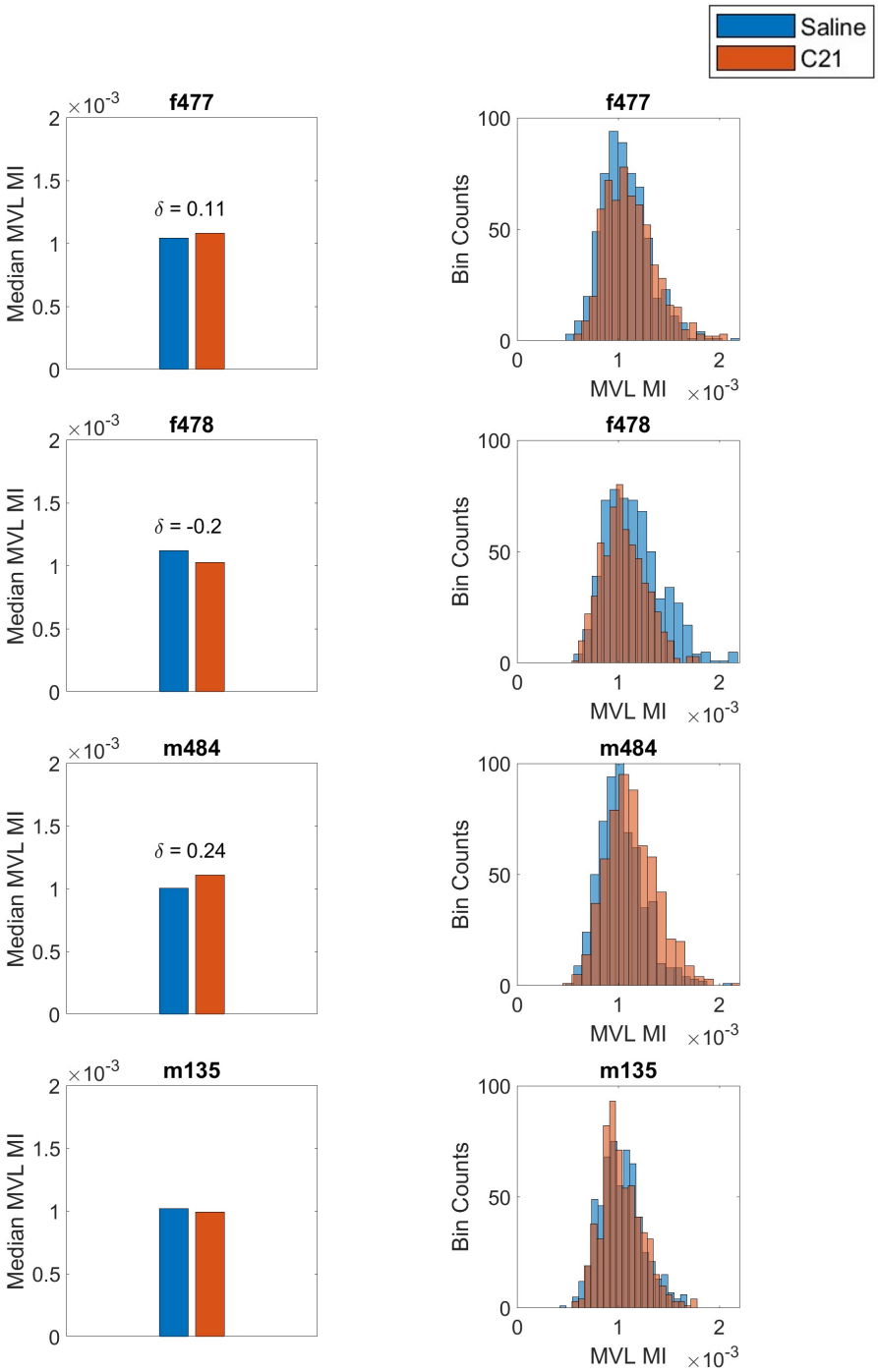


**Figure 3.11:** Medians and histograms of time-frequency averaged MVL MI values. Both plots were constructed by joining the PAC estimates from both hippocampi together into one vector, thus getting the medians/histograms of PAC estimates for the hippocampus as a whole. Cliff's $\delta$ is displayed above each bar plot where the difference was significant ($p < 0.05$).

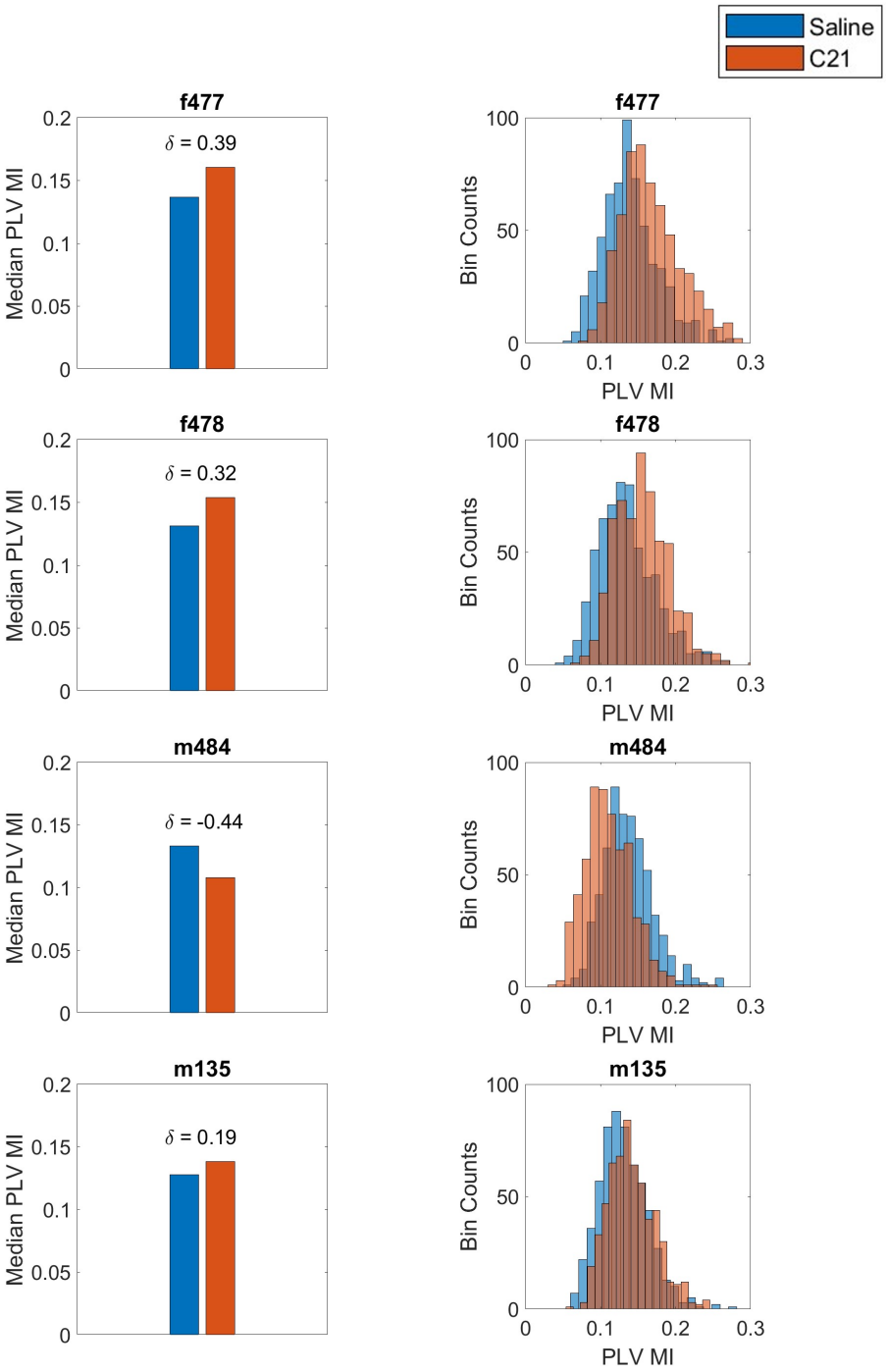


**Figure 3.12:** Medians and histograms of time-frequency averaged PLV MI values. Otherwise same as Figure 3.11. PLV MI PAC estimates showed significant differences between saline/C21 recordings in all animals, but again not always in the same direction. Effect size is displayed above each bar plot.

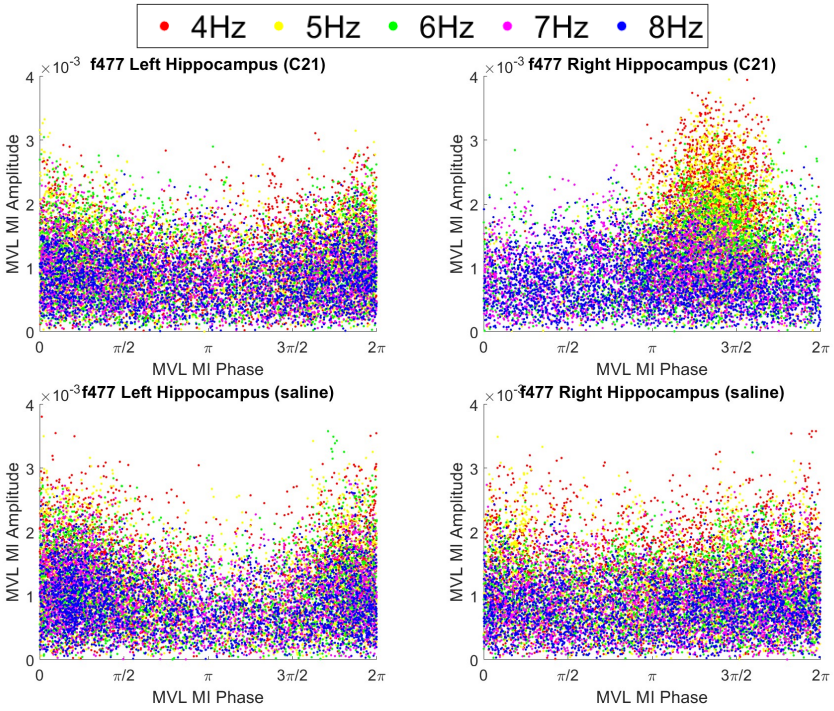


**Figure 3.13:** MVL MI Phase-amplitude plots showing the potential phase offset preference in theta-gamma PAC. Phase was extracted from the complex vector in Equation 2.11, while the amplitude is the MVL MI value itself. In most cases, the distribution looks uniform, with decreases around $\pi$. When there is a notable increase in the MVL MI amplitude, it is usually for phases around $\frac{3\pi}{2}$. The increases are visible mostly for lower theta frequencies.

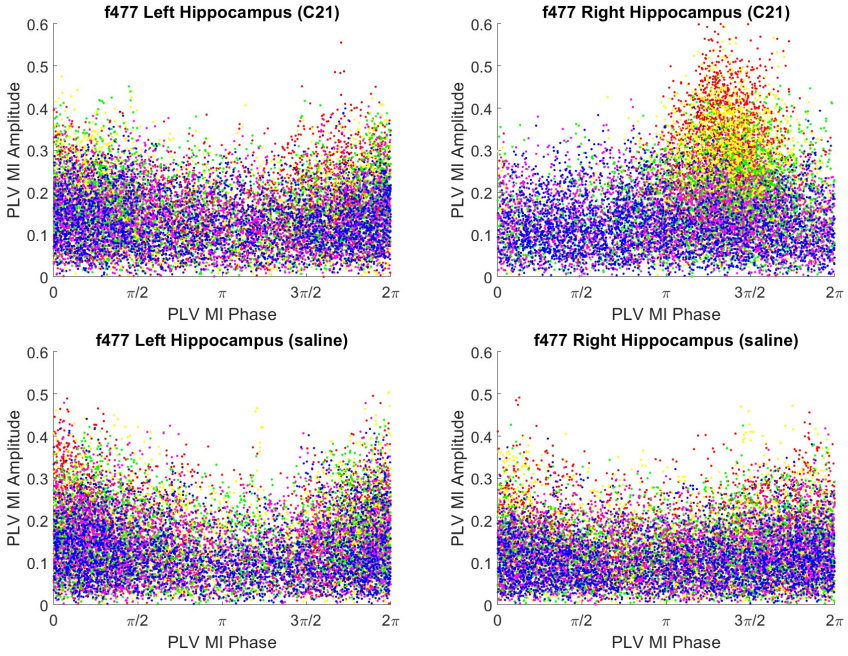


**Figure 3.14:** PLV MI Phase-amplitude plots. Otherwise same as Figure 3.13. Results from both methods are comparable.

# Chapter 4

# Discussion

Cross-frequency coupling (CFC) has long been proposed as an important mechanism for coordinated communication between neuronal groups and across brain regions. Changes in coupling may also be used to detect early signs of neurological or neuropsychological diseases [48], [46]. Having reliable tools for the detection of coupling is essential for advancing our understanding of how the brain functions. Here, I have focused on hippocampal theta-gamma (4-8Hz to 50-70Hz) phase-amplitude coupling (PAC). This synchronization is believed to facilitate the coordination of neuronal activity during cognitive tasks, such as spatial navigation, memory encoding/retrieval, while disruptions thereof can impact learning and memory processes. As an example, such pathological changes in PAC were previously reported in rat and mice models of Alzheimer's disease [42], [43].

For the evaluation of PAC, I employed two modulation indices, MVL MI and PLV MI, as well as wavelet coherence. Subsequently, I used these modulation indices to detect changes in PAC in PV-Cre transgenic mice before and after brain-wide chemogenetic activation of parvalbumin (PV) interneurons under urethane anesthesia (injection of saline followed by injection of C21, onwards I refer to the LFP data as saline/C21 recordings).

## 4.1 Method Comparison on Simulated Data

The comparison of methods on surrogate data was qualitative but clearly displayed their behavior. For a quantitative comparison, I cited previous works that employed more sophisticated techniques for generating surrogate data, rather than the simple multiplication of sinusoids used here [70], [69]. The authors generally suggest, that there is no single optimal method, and the choice should be based on experiment design and recording quality. All three methods were able to detect simulated PAC, but wavelet coherence achieved worse frequency resolution compared to the modulation indices (MIs). This discrepancy is likely due to the double application of CWT to obtain coherence values, which leads to further blurring in time and frequency. Another factor could be the normalization in wavelet coherence (denominator of Equation 2.13). The wavelet cross-spectrum, which does not use this normalization, showed results more similar to the MIs. I expect

wavelet coherence to perform better when used for determining CFC across electrodes, similar to phase-phase coupling methods, rather than for the single electrode PAC approach demonstrated here.

The MIs were similar in terms of frequency resolution and sensitivity to noise, and my results are comparable to those in other works [69], [70]. It's possible that using a traditional filter bank might yield slightly better resolution than the wavelets I used due to sharper frequency cutoffs. Consistent with previous literature, setting the time window for MIs below 1000ms results in inflated PAC estimates when there is no coupling present [70]. To my knowledge, there is no standard for the optimal time window. Here, I used a fixed window for each lower frequency, as is commonly done. This approach grants slower oscillations better time resolution at the expense of frequency resolution and vice versa for higher frequencies [61]. To illustrate, the 2000ms window corresponds to (8, 10, 12, 14, 16) cycles of the respective 4-8Hz oscillations. Therefore, to reach a large MI value for 8Hz coupled some higher frequency, there would need to be sustained coupling for close to 16 cycles of the 8Hz oscillation, which seems unlikely in real recordings. It might be worth varying the time window based on the lower frequency examined, similar to how CWT changes scales. For example, if one chose 8 cycles, that would result in windows of approximately (2, 1.6, 1.3, 1.14, 1) seconds for 4-8Hz oscillations, potentially giving the MIs equal chance of detecting events of sustained 8-cycle coupling. Even so, now the question of how to choose the time window would change to selecting the optimal number of cycles, and I doubt a simple answer exists.

## 4.2 Interpretation of Results from LFP Recordings

Hippocampal theta-gamma PAC of the respective saline/C21 recordings showed significant differences in most animals, but not in a consistent way. Mainly, PAC was greater after chemogenetic activation of PV interneurons, but in some cases, saline recordings displayed stronger coupling. In case of MVL MI, coupling was greater in C21 recordings of two animals, while the reverse was true for one animal. For PLV MI, three animals showed increased coupling after injection of C21 and one on saline, possibly suggesting that PLV MI is more sensitive for our data. Activity of PV interneurons plays a pivotal role in formation of theta and gamma oscillations in the hippocampus, and altering their activity can lead to changes in either rhythm, as well as coupling between them [25], [29], [75].

Here, the activation of PV interneurons likely accounts for some changes in PAC, but it's also necessary to consider other factors, such as the choice of recording segment for analysis. The C21 recordings were conducted only after the initial 50 minute saline recording, and the last 10 minutes of these recordings were selected for analysis. Sleep-like rapid/non-rapid eye movement (REM/nREM) patterns appear in rats anesthetized with urethane [76]. REM stages are characterized by rhythmic theta activity, while nREM is characterized by large amplitude slow wave activity ($< 4$Hz). If one state

is prominent in the saline recording and the other in the C21 recording, it could lead to significant differences in PAC. Urethane anesthesia itself also leads to a decreased synchronization of activity of hippocampal neurons [77]. C21 recordings were conducted after 50 minutes of saline recordings, so it's possible the effects of prolonged anesthesia also influenced the results.

The observed increased modulation of hippocampal gamma amplitude near theta troughs is consistent with previous works [29], [62], [68], [61]. The theta trough seems to be a period heightened excitability for cells which generate the gamma rhythm (including PV interneurons). This potentially ties in with the work of Fries and his Communication through Coherence hypothesis. Theta oscillations may create windows of excitation and inhibition in the hippocampus, and gamma activity generated by cells not aligned with these windows is silenced [30], [19].

## 4.3 Future Prospects and Limitations

In upcoming work, I'd ideally conduct similar analysis for a greater number of subjects than the four animals examined here. To avoid the mentioned ambiguities tied with selecting only the last 10 minutes of each recording, it seems appropriate to also examine the whole 50 minute recording. This would allow for tracking changes in PAC as the injected compound takes effect. This is necessary for the saline recordings as well in order to distinguish effects of urethane anesthesia from those brought on by increased interneuron activity.

Naturally, analyzing more and longer recordings increases the computational time. Since I had a control recording for each animal, I was able to compare the differences in distributions of MI values from saline/C21 recordings. For experimental designs without direct control recordings, significance values for each coupling estimate are usually calculated via bootstrapping techniques. This involves thresholding each value by some percentage from a surrogate distribution of PAC estimates at each time point, constructed by repeatedly shuffling phase values of the studied segment and calculating MIs for it (usually hundreds of iterations) [78]. This step increases computation time several hundred-fold, which is impractical for exploratory analysis of long signals. Therefore, it might be better to choose a threshold, such as the median or another percentile. While this approach introduces the arbitrary choice of a threshold, the standard approach might simply not be feasible.

Lastly, I've examined only PAC for a limited theta-gamma range in the hippocampus. In the future, I'd like to exted my focus to cross-regional PAC and phase-phase coupling to gain a more comprehensive understanding of how CFC patterns relate to neurophysiological processes.

# Chapter 5

# Conclusion

I have qualitatively examined methods for estimation of PAC, namely the wavelet coherence, MVL MI and PLV MI on simulated data. All three methods are capable of detecting coupling and their time resolution was comparable. The manner in which I used wavelet coherence for the detection of PAC showed worse frequency resolution than the modulation indices.

For the analysis of electrophysiological recordings from PV-Cre mice, I detected increases hippocampal theta-gamma (4-8Hz to 50-70Hz) PAC after brain-wide chemogenetic activation of PV interneurons in most animals, but the results were not entirely consistent. To draw firm conclusions, increasing the sample size and conducting further analyses is necessary. With this, I believe to have fulfilled all aspects of the assigned task, but the presented results should be considered preliminary.

# Bibliography


[1] Liset Menendez de la Prida and Gilles Huberfeld. Inhibition and oscillations in the human brain tissue in vitro. *Neurobiology of Disease*, 125:198–210, May 2019. ISSN 0969-9961. doi: 10.1016/j.nbd.2019.02.006. URL https://www.sciencedirect.com/science/article/pii/S0969996118307344.

[2] Herbert Jasper and Wilder Penfield. Electrocorticograms in man: Effect of voluntary movement upon the electrical activity of the precentral gyrus. *Archiv for Psychiatrie und Nervenkrankheiten*, 183(1-2):163–174, 1949. ISSN 0003-9373, 1433-8491. doi: 10.1007/BF01062488. URL http://link.springer.com/10.1007/BF01062488.

[3] Craig G. Richter, William H. Thompson, Conrado A. Bosman, and Pascal Fries. Top-Down Beta Enhances Bottom-Up Gamma. *The Journal of Neuroscience*, 37(28):6698–6711, July 2017. ISSN 0270-6474, 1529-2401. doi: 10.1523/JNEUROSCI.3771-16.2017. URL https://www.jneurosci.org/lookup/doi/10.1523/JNEUROSCI.3771-16.2017.

[4] Joshua Jacobs. Hippocampal theta oscillations are slower in humans than in rodents: implications for models of spatial navigation and memory. *Philosophical Transactions of the Royal Society B: Biological Sciences*, 369(1635):20130304, February 2014. ISSN 0962-8436. doi: 10.1098/rstb.2013.0304. URL https://www.ncbi.nlm.nih.gov/pmc/articles/PMC3866455/.

[5] Keith B. Doelling and M. Florencia Assaneo. Neural oscillations are a start toward understanding brain activity rather than the end. *PLoS Biology*, 19(5):e3001234, May 2021. ISSN 1544-9173. doi: 10.1371/journal.pbio.3001234. URL https://www.ncbi.nlm.nih.gov/pmc/articles/PMC8121326/.

[6] Espen Hagen, Solveig Næss, Torbjørn V. Ness, and Gaute T. Einevoll. Multimodal Modeling of Neural Network Activity: Computing LFP, ECoG, EEG, and MEG Signals With LFPy 2.0. *Frontiers in Neuroinformatics*, 12, December 2018. ISSN 1662-5196. doi: 10.3389/fninf.2018.00092. URL https://www.frontiersin.org/articles/10.3389/fninf.2018.00092. Publisher: Frontiers.

[7] Thalía Harmony. The functional significance of delta oscillations in cognitive processing. *Frontiers in Integrative Neuroscience*, 7:83, December 2013. ISSN 1662-5145. doi: 10.3389/fnint.2013.00083. URL https://www.ncbi.nlm.nih.gov/pmc/articles/PMC3851789/.

[8] Siyu Long, Rui Ding, Junce Wang, Yue Yu, Jing Lu, and Dezhong Yao. Sleep Quality and Electroencephalogram Delta Power. *Frontiers in Neuroscience*, 15:803507, December 2021. ISSN 1662-4548. doi: 10.3389/fnins.2021.803507. URL https://www.ncbi.nlm.nih.gov/pmc/articles/PMC8715081/.

[9] Thalía Fernández, Thalía Harmony, Mario Rodríguez, Jorge Bernal, Juan Silva, Alfonso Reyes, and Erzsébet Marosi. EEG activation patterns during the performance of tasks involving different components of mental calculation. *Electroencephalography and Clinical Neurophysiology*, 94 (3):175–182, March 1995. ISSN 0013-4694. doi: 10.1016/0013-4694(94)00262-J. URL https://www.sciencedirect.com/science/article/pii/001346949400262J.

[10] Ralitsa Todorova and Michaël Zugaro. Isolated cortical computations during delta waves support memory consolidation. *Science (New York, N.Y.)*, 366(6463):377–381, October 2019. ISSN 1095-9203. doi: 10.1126/science.aay0616.

[11] Angel Nuñez and Washington Buño. The Theta Rhythm of the Hippocampus: From Neuronal and Circuit Mechanisms to Behavior. *Frontiers in Cellular Neuroscience*, 15:649262, March 2021. ISSN 1662-5102. doi: 10.3389/fncel.2021.649262. URL https://www.frontiersin.org/articles/10.3389/fncel.2021.649262/full.

[12] György Buzsáki. Theta Oscillations in the Hippocampus. *Neuron*, 33(3):325–340, January 2002. ISSN 0896-6273. doi: 10.1016/S0896-6273(02)00586-X. URL https://www.cell.com/neuron/abstract/S0896-6273(02)00586-X. Publisher: Elsevier.

[13] Pascal Fries. Rhythmic attentional scanning. *Neuron*, 111(7):954–970, April 2023. ISSN 08966273. doi: 10.1016/j.neuron.2023.02.015. URL https://linkinghub.elsevier.com/retrieve/pii/S0896627323001198.

[14] Norbert J. Fortin, Kara L. Agster, and Howard B. Eichenbaum. Critical role of the hippocampus in memory for sequences of events. *Nature neuroscience*, 5(5):458–462, May 2002. ISSN 1097-6256. doi: 10.1038/nn834. URL https://www.ncbi.nlm.nih.gov/pmc/articles/PMC4053170/.

[15] Michael E. Hasselmo, Clara Bodelón, and Bradley P. Wyble. A proposed function for hippocampal theta rhythm: separate phases of encoding and retrieval enhance reversal of prior learning. *Neural Computation*, 14(4):793–817, April 2002. ISSN 0899-7667. doi: 10.1162/089976602317318965.

[16] Casper Kerrén, Juan Linde-Domingo, Simon Hanslmayr, and Maria Wimber. An Optimal Oscillatory Phase for Pattern Reactivation during Memory Retrieval. *Current biology: CB*, 28(21):3383–3392.e6, November 2018. ISSN 1879-0445. doi: 10.1016/j.cub.2018.08.065.

[17] Wolfgang Klimesch. Alpha-band oscillations, attention, and controlled access to stored information. *Trends in Cognitive Sciences*, 16(12):606–617, December 2012. ISSN 1364-6613, 1879-307X. doi: 10.1016/j.tics.2012.10.007. URL `https://www.cell.com/trends/cognitive-sciences/abstract/S1364-6613(12)00243-4`. Publisher: Elsevier.

[18] John J. Foxe and Adam C. Snyder. The Role of Alpha-Band Brain Oscillations as a Sensory Suppression Mechanism during Selective Attention. *Frontiers in Psychology*, 2, 2011. ISSN 1664-1078. doi: 10.3389/fpsyg.2011.00154. URL `http://journal.frontiersin.org/article/10.3389/fpsyg.2011.00154/abstract`.

[19] Pascal Fries. Rhythms For Cognition: Communication Through Coherence. *Neuron*, 88(1):220–235, October 2015. ISSN 0896-6273. doi: 10.1016/j.neuron.2015.09.034. URL `https://www.ncbi.nlm.nih.gov/pmc/articles/PMC4605134/`.

[20] Jacopo Barone and Holly E. Rossiter. Understanding the Role of Sensorimotor Beta Oscillations. *Frontiers in Systems Neuroscience*, 15, May 2021. ISSN 1662-5137. doi: 10.3389/fnsys.2021.655886. URL `https://www.frontiersin.org/articles/10.3389/fnsys.2021.655886`. Publisher: Frontiers.

[21] O. Jensen, P. Goel, N. Kopell, M. Pohja, R. Hari, and B. Ermentrout. On the human sensorimotor-cortex beta rhythm: sources and modeling. *NeuroImage*, 26(2):347–355, June 2005. ISSN 1053-8119. doi: 10.1016/j.neuroimage.2005.02.008.

[22] Alejo J. Nevado Holgado, John R. Terry, and Rafal Bogacz. Conditions for the generation of beta oscillations in the subthalamic nucleus-globus pallidus network. *The Journal of Neuroscience: The Official Journal of the Society for Neuroscience*, 30(37):12340–12352, September 2010. ISSN 1529-2401. doi: 10.1523/JNEUROSCI.0817-10.2010.

[23] György Buzsáki and Brendon O. Watson. Brain rhythms and neural syntax: implications for efficient coding of cognitive content and neuropsychiatric disease. *Dialogues in Clinical Neuroscience*, 14(4):345–367, December 2012. ISSN 1958-5969. doi: 10.31887/DCNS.2012.14.4/gbuzsaki. URL `https://www.tandfonline.com/doi/full/10.31887/DCNS.2012.14.4/gbuzsaki`.

[24] Ao Guan, Shaoshuang Wang, Ailing Huang, Chenyue Qiu, Yansong Li, Xuying Li, Jinfei Wang, Qiang Wang, and Bin Deng. The role of gamma oscillations in central nervous system diseases: Mechanism and

treatment. *Frontiers in Cellular Neuroscience*, 16, July 2022. ISSN 1662-5102. doi: 10.3389/fncel.2022.962957. URL https://www.frontiersin.org/articles/10.3389/fncel.2022.962957. Publisher: Frontiers.

[25] Marlene Bartos, Imre Vida, and Peter Jonas. Synaptic mechanisms of synchronized gamma oscillations in inhibitory interneuron networks. *Nature Reviews Neuroscience*, 8(1):45–56, January 2007. ISSN 1471-0048. doi: 10.1038/nrn2044. URL https://www.nature.com/articles/nrn2044. Publisher: Nature Publishing Group.

[26] L. López-Aguado, J. M. Ibarz, P. Varona, and O. Herreras. Structural Inhomogeneities Differentially Modulate Action Currents and Population Spikes Initiated in the Axon or Dendrites. *Journal of Neurophysiology*, 88(5):2809–2820, November 2002. ISSN 0022-3077. doi: 10.1152/jn.00183.2002. URL https://journals.physiology.org/doi/full/10.1152/jn.00183.2002. Publisher: American Physiological Society.

[27] R. LORENTE de NO. Analysis of the distribution of the action currents of nerve in volume conductors. *Studies from the Rockefeller Institute for Medical Research. Reprints. Rockefeller Institute for Medical Research*, 132:384–477, 1947.

[28] György Buzsáki and Xiao-Jing Wang. Mechanisms of Gamma Oscillations. *Annual review of neuroscience*, 35:203–225, 2012. ISSN 0147-006X. doi: 10.1146/annurev-neuro-062111-150444. URL https://www.ncbi.nlm.nih.gov/pmc/articles/PMC4049541/.

[29] Bénédicte Amilhon, Carey Y. L. Huh, Frédéric Manseau, Guillaume Ducharme, Heather Nichol, Antoine Adamantidis, and Sylvain Williams. Parvalbumin Interneurons of Hippocampus Tune Population Activity at Theta Frequency. *Neuron*, 86(5):1277–1289, June 2015. ISSN 1097-4199. doi: 10.1016/j.neuron.2015.05.027.

[30] Pascal Fries. A mechanism for cognitive dynamics: neuronal communication through neuronal coherence. *Trends in Cognitive Sciences*, 9(10):474–480, October 2005. ISSN 13646613. doi: 10.1016/j.tics.2005.08.011. URL https://linkinghub.elsevier.com/retrieve/pii/S1364661305002421.

[31] Mark J. Roberts, Eric Lowet, Nicolas M. Brunet, Marije Ter Wal, Paul Tiesinga, Pascal Fries, and Peter De Weerd. Robust Gamma Coherence between Macaque V1 and V2 by Dynamic Frequency Matching. *Neuron*, 78(3):523–536, May 2013. ISSN 08966273. doi: 10.1016/j.neuron.2013.03.003. URL https://linkinghub.elsevier.com/retrieve/pii/S0896627313002274.

[32] Ryan T. Canolty and Robert T. Knight. The functional role of cross-frequency coupling. *Trends in Cognitive Sciences*, 14(11):506–515, November 2010. ISSN 13646613. doi: 10.1016/j.tics.2010.

09.001. URL https://linkinghub.elsevier.com/retrieve/pii/S1364661310002068.

[33] Bradley Voytek, Ryan T. Canolty, Avgusta Shestyuk, Nathan Crone, Josef Parvizi, and Robert T. Knight. Shifts in Gamma Phase–Amplitude Coupling Frequency from Theta to Alpha Over Posterior Cortex During Visual Tasks. *Frontiers in Human Neuroscience*, 4, October 2010. ISSN 1662-5161. doi: 10.3389/fnhum.2010.00191. URL https://www.frontiersin.org/articles/10.3389/fnhum.2010.00191. Publisher: Frontiers.

[34] Maciej Kaminski, Aneta Brzezicka, Jan Kaminski, and Katarzyna J. Blinowska. Coupling Between Brain Structures During Visual and Auditory Working Memory Tasks. *International Journal of Neural Systems*, March 2019. doi: 10.1142/S0129065718500466. URL https://www.worldscientific.com/worldscinet/ijns. Publisher: World Scientific Publishing Company.

[35] Alexandre Hyafil, Anne-Lise Giraud, Lorenzo Fontolan, and Boris Gutkin. Neural Cross-Frequency Coupling: Connecting Architectures, Mechanisms, and Functions. *Trends in Neurosciences*, 38(11):725–740, November 2015. ISSN 01662236. doi: 10.1016/j.tins.2015.09.001. URL https://linkinghub.elsevier.com/retrieve/pii/S0166223615002088.

[36] Robson Scheffer-Teixeira and Adriano Bl Tort. On cross-frequency phase-phase coupling between theta and gamma oscillations in the hippocampus. *eLife*, 5:e20515, December 2016. ISSN 2050-084X. doi: 10.7554/eLife.20515.

[37] Georgia G. Gregoriou, Stephen J. Gotts, Huihui Zhou, and Robert Desimone. High-frequency, long-range coupling between prefrontal and visual cortex during attention. *Science (New York, N.Y.)*, 324(5931):1207–1210, May 2009. ISSN 0036-8075. doi: 10.1126/science.1171402. URL https://www.ncbi.nlm.nih.gov/pmc/articles/PMC2849291/.

[38] Joaquín González, Matias Cavelli, Alejandra Mondino, Nicolás Rubido, BL Tort, and Pablo Torterolo. Communication through coherence by means of cross-frequency coupling.

[39] N Rabino. Analysis and Qualitative Effects of Large Breasts on Aerodynamic Performance and Wake of a "Miss Kobayashi's Dragon Maid" Character, 2018. URL http://rgdoi.net/10.13140/RG.2.2.30181.50404/1.

[40] Yousef Salimpour and William S. Anderson. Cross-Frequency Coupling Based Neuromodulation for Treating Neurological Disorders. *Frontiers in Neuroscience*, 13, February 2019. ISSN 1662-453X. doi: 10.3389/fnins.2019.00125. URL https://www.frontiersin.org/journals/neuroscience/articles/10.3389/fnins.2019.00125/full. Publisher: Frontiers.

[41] Daniella B Victorino, Jean Faber, Daniel J. L. L Pinheiro, Fulvio A Scorza, Antônio C. G Almeida, Alberto C. S Costa, and Carla A Scorza. Toward the Identification of Neurophysiological Biomarkers for Alzheimer's Disease in Down Syndrome: A Potential Role for Cross-Frequency Phase-Amplitude Coupling Analysis. *Aging and Disease*, 14 (2):428–449, April 2023. ISSN 2152-5250. doi: 10.14336/AD.2022.0906. URL https://www.ncbi.nlm.nih.gov/pmc/articles/PMC10017148/.

[42] Paolo Bazzigaluppi, Tina L. Beckett, Margaret M. Koletar, Aaron Y. Lai, Illsung L. Joo, Mary E. Brown, Peter L. Carlen, JoAnne McLaurin, and Bojana Stefanovic. Early-stage attenuation of phase-amplitude coupling in the hippocampus and medial prefrontal cortex in a transgenic rat model of Alzheimer's disease. *Journal of Neurochemistry*, 144(5):669–679, 2018. ISSN 1471-4159. doi: 10.1111/jnc.14136. URL https://onlinelibrary.wiley.com/doi/abs/10.1111/jnc.14136. _eprint: https://onlinelibrary.wiley.com/doi/pdf/10.1111/jnc.14136.

[43] Romain Goutagny, Ning Gu, Chelsea Cavanagh, Jesse Jackson, Jean-Guy Chabot, Rémi Quirion, Slavica Krantic, and Sylvain Williams. Alterations in hippocampal network oscillations and theta–gamma coupling arise before AB overproduction in a mouse model of Alzheimer's disease. *European Journal of Neuroscience*, 37(12):1896–1902, 2013. ISSN 1460-9568. doi: 10.1111/ejn.12233. URL https://onlinelibrary.wiley.com/doi/abs/10.1111/ejn.12233. _eprint: https://onlinelibrary.wiley.com/doi/pdf/10.1111/ejn.12233.

[44] Guglielmo Foffani and Manuel Alegre. Chapter 18 - Brain oscillations and Parkinson disease. In Angelo Quartarone, Maria Felice Ghilardi, and François Boller, editors, *Handbook of Clinical Neurology*, volume 184 of *Neuroplasticity*, pages 259–271. Elsevier, January 2022. doi: 10.1016/B978-0-12-819410-2.00014-X. URL https://www.sciencedirect.com/science/article/pii/B978012819410200014X.

[45] Mark Witcher, Rosalyn Moran, Stephen B. Tatter, and Adrian W. Laxton. Neuronal oscillations in Parkinson's disease. *Frontiers in Bioscience-Landmark*, 19(8):1291–1299, June 2014. ISSN 2768-6701. doi: 10.2741/4282. URL https://www.imrpress.com/journal/FBL/19/8/10.2741/4282. Number: 8 Publisher: IMR Press.

[46] Coralie de Hemptinne, Elena S. Ryapolova-Webb, Ellen L. Air, Paul A. Garcia, Kai J. Miller, Jeffrey G. Ojemann, Jill L. Ostrem, Nicholas B. Galifianakis, and Philip A. Starr. Exaggerated phase–amplitude coupling in the primary motor cortex in Parkinson disease. *Proceedings of the National Academy of Sciences*, 110(12):4780–4785, March 2013. doi: 10.1073/pnas.1214546110. URL https://www.pnas.org/doi/full/10.1073/pnas.1214546110. Publisher: Proceedings of the National Academy of Sciences.

[47] Ruxue Gong, Mirko Wegscheider, Christoph Mühlberg, Richard Gast, Christopher Fricke, Jost-Julian Rumpf, Vadim V. Nikulin, Thomas R. Knösche, and Joseph Classen. Spatiotemporal features of $\beta$-$\gamma$ phase-amplitude coupling in Parkinson's disease derived from scalp EEG. *Brain: A Journal of Neurology*, 144(2):487–503, March 2021. ISSN 1460-2156. doi: 10.1093/brain/awaa400.

[48] Mera S. Barr, Tarek K. Rajji, Reza Zomorrodi, Natasha Radhu, Tony P. George, Daniel M. Blumberger, and Zafiris J. Daskalakis. Impaired theta-gamma coupling during working memory performance in schizophrenia. *Schizophrenia Research*, 189:104–110, November 2017. ISSN 1573-2509. doi: 10.1016/j.schres.2017.01.044.

[49] Kenji Kirihara, Anthony J. Rissling, Neal R. Swerdlow, David L. Braff, and Gregory A. Light. Hierarchical Organization of Gamma and Theta Oscillatory Dynamics in Schizophrenia. *Biological psychiatry*, 71(10):873–880, May 2012. ISSN 0006-3223. doi: 10.1016/j.biopsych.2012.01.016. URL `https://www.ncbi.nlm.nih.gov/pmc/articles/PMC3434875/`.

[50] John D. Rolston, David Ouyang, Dario J. Englot, Doris D. Wang, and Edward F. Chang. National trends and complication rates for invasive extraoperative electrocorticography in the USA. *Journal of clinical neuroscience : official journal of the Neurosurgical Society of Australasia*, 22 (5):823–827, May 2015. ISSN 0967-5868. doi: 10.1016/j.jocn.2014.12.002. URL `https://www.ncbi.nlm.nih.gov/pmc/articles/PMC5501272/`.

[51] Bernice Bovenkerk and Frederike Kaldewaij. The use of animal models in behavioural neuroscience research. *Current Topics in Behavioral Neurosciences*, 19:17–46, 2015. ISSN 1866-3370. doi: 10.1007/7854_2014_329.

[52] Witold Żakowski. Animal Use in Neurobiological Research. *Neuroscience*, 433:1–10, May 2020. ISSN 0306-4522. doi: 10.1016/j.neuroscience.2020.02.049. URL `https://www.sciencedirect.com/science/article/pii/S0306452220301421`.

[53] Robert M. Cohen, Kavon Rezai-Zadeh, Tara M. Weitz, Altan Rentsendorj, David Gate, Inna Spivak, Yasmin Bholat, Vitaly Vasilevko, Charles G. Glabe, Joshua J. Breunig, Pasko Rakic, Hayk Davtyan, Michael G. Agadjanyan, Vladimir Kepe, Jorge R. Barrio, Serguei Bannykh, Christine A. Szekely, Robert N. Pechnick, and Terrence Town. A Transgenic Alzheimer Rat with Plaques, Tau Pathology, Behavioral Impairment, Oligomeric AB, and Frank Neuronal Loss. *The Journal of Neuroscience*, 33(15):6245–6256, April 2013. ISSN 0270-6474, 1529-2401. doi: 10.1523/JNEUROSCI.3672-12.2013. URL `https://www.jneurosci.org/lookup/doi/10.1523/JNEUROSCI.3672-12.2013`.

[54] CA Jones, DJG Watson, and KCF Fone. Animal models of schizophrenia. *British Journal of Pharmacology*, 164(4):1162–1194, October 2011. ISSN

0007-1188. doi: 10.1111/j.1476-5381.2011.01386.x. URL https://www.ncbi.nlm.nih.gov/pmc/articles/PMC3229756/.

[55] Elena A. Konnova and Maria Swanberg. Animal Models of Parkinson's Disease. In Thomas B. Stoker and Julia C. Greenland, editors, *Parkinson's Disease: Pathogenesis and Clinical Aspects*. Codon Publications, Brisbane (AU), 2018. ISBN 978-0-9944381-6-4. URL http://www.ncbi.nlm.nih.gov/books/NBK536725/.

[56] Oscar Herreras. Local Field Potentials: Myths and Misunderstandings. *Frontiers in Neural Circuits*, 10, December 2016. ISSN 1662-5110. doi: 10.3389/fncir.2016.00101. URL https://www.frontiersin.org/articles/10.3389/fncir.2016.00101. Publisher: Frontiers.

[57] Steffen Katzner, Ian Nauhaus, Andrea Benucci, Vincent Bonin, Dario L. Ringach, and Matteo Carandini. Local origin of field potentials in visual cortex. *Neuron*, 61(1):35–41, January 2009. ISSN 0896-6273. doi: 10.1016/j.neuron.2008.11.016. URL https://www.ncbi.nlm.nih.gov/pmc/articles/PMC2730490/.

[58] A. Schüz and G. Palm. Density of neurons and synapses in the cerebral cortex of the mouse. *The Journal of Comparative Neurology*, 286(4): 442–455, August 1989. ISSN 0021-9967. doi: 10.1002/cne.902860404.

[59] Lan Luan, Xiaoling Wei, Zhengtuo Zhao, Jennifer J. Siegel, Ojas Potnis, Catherine A. Tuppen, Shengqing Lin, Shams Kazmi, Robert A. Fowler, Stewart Holloway, Andrew K. Dunn, Raymond A. Chitwood, and Chong Xie. Ultraflexible nanoelectronic probes form reliable, glial scar-free neural integration. *Science Advances*, 3(2):e1601966, February 2017. ISSN 2375-2548. doi: 10.1126/sciadv.1601966.

[60] Bijan Pesaran, Martin Vinck, Gaute T. Einevoll, Anton Sirota, Pascal Fries, Markus Siegel, Wilson Truccolo, Charles E. Schroeder, and Ramesh Srinivasan. Investigating large-scale brain dynamics using field potential recordings: analysis and interpretation. *Nature Neuroscience*, 21(7): 903–919, July 2018. ISSN 1546-1726. doi: 10.1038/s41593-018-0171-8.

[61] Michael X Cohen. Assessing transient cross-frequency coupling in EEG data. *Journal of Neuroscience Methods*, 168(2):494–499, March 2008. ISSN 0165-0270. doi: 10.1016/j.jneumeth.2007.10.012. URL https://www.sciencedirect.com/science/article/pii/S0165027007005237.

[62] Bradley Lega, John Burke, Joshua Jacobs, and Michael J. Kahana. Slow-Theta-to-Gamma Phase–Amplitude Coupling in Human Hippocampus Supports the Formation of New Episodic Memories. *Cerebral Cortex*, 26 (1):268–278, January 2016. ISSN 1047-3211. doi: 10.1093/cercor/bhu232. URL https://doi.org/10.1093/cercor/bhu232.

[63] George Paxinos and Keith B. J. Franklin. *Paxinos and Franklin's The mouse brain in stereotaxic coordinates*. Elsevier, Academic Press, London San Diego Cambridge; MA Kidlington, Oxford, fifth edition edition, 2019. ISBN 978-0-12-816157-9.

[64] MathWorks, Inc. MATLAB `hilbert()` function. `https://www.mathworks.com/help/signal/ref/hilbert.html`, . Accessed: 2024-04-13.

[65] S.C. Olhede and A.T. Walden. Generalized Morse wavelets. *IEEE Transactions on Signal Processing*, 50(11):2661–2670, November 2002. ISSN 1053-587X. doi: 10.1109/TSP.2002.804066. URL `http://ieeexplore.ieee.org/document/1041025/`.

[66] MathWorks, Inc. MATLAB `cwt()` function. `https://www.mathworks.com/help/wavelet/ref/cwt.html`, . Accessed: 2024-04-25.

[67] MathWorks, Inc. MATLAB `cwtfilterbank()` function. `https://www.mathworks.com/help/wavelet/ref/cwtfilterbank.html`, . Accessed: 2024-04-25.

[68] R. T. Canolty, E. Edwards, S. S. Dalal, M. Soltani, S. S. Nagarajan, H. E. Kirsch, M. S. Berger, N. M. Barbaro, and R. T. Knight. High Gamma Power Is Phase-Locked to Theta Oscillations in Human Neocortex. *Science (New York, N.Y.)*, 313(5793):1626–1628, September 2006. ISSN 0036-8075. doi: 10.1126/science.1128115. URL `https://www.ncbi.nlm.nih.gov/pmc/articles/PMC2628289/`.

[69] Tolga Esat Özkurt and Alfons Schnitzler. A critical note on the definition of phase–amplitude cross-frequency coupling. *Journal of Neuroscience Methods*, 201(2):438–443, October 2011. ISSN 0165-0270. doi: 10.1016/j.jneumeth.2011.08.014. URL `https://www.sciencedirect.com/science/article/pii/S0165027011004730`.

[70] Robert Seymour, Gina Rippon, and Klaus Kessler. The Detection of Phase Amplitude Coupling during Sensory Processing. *Frontiers in Neuroscience*, 11:487, September 2017. doi: 10.3389/fnins.2017.00487.

[71] MathWorks, Inc. MATLAB `wcoherence()` function. `https://www.mathworks.com/help/wavelet/ref/wcoherence.html`, . Accessed: 2024-04-25.

[72] MathWorks, Inc. MATLAB `meaneffectsize()` function. `https://www.mathworks.com/help/stats/meaneffectsize.html`, . Accessed: 2024-05-11.

[73] Norman Cliff. Dominance statistics: Ordinal analyses to answer ordinal questions. *Psychological Bulletin*, 114(3):494–509, November 1993. ISSN 1939-1455, 0033-2909. doi: 10.1037/0033-2909.114.3.494. URL `https://doi.apa.org/doi/10.1037/0033-2909.114.3.494`.

[74] MathWorks, Inc. MATLAB `ranksum()` function. `https://www.mathworks.com/help/stats/ranksum.html`, . Accessed: 2024-05-11.

[75] Kyerl Park, Jaedong Lee, Hyun Jae Jang, Blake A. Richards, Michael M. Kohl, and Jeehyun Kwag. Optogenetic activation of parvalbumin and somatostatin interneurons selectively restores theta-nested gamma oscillations and oscillation-induced spike timing-dependent long-term potentiation impaired by amyloid beta oligomers. *BMC Biology*, 18(1):7, December 2020. ISSN 1741-7007. doi: 10.1186/s12915-019-0732-7. URL `https://bmcbiol.biomedcentral.com/articles/10.1186/s12915-019-0732-7`.

[76] Alejandra Mondino, Joaquín González, Duan Li, Diego Mateos, Lucía Osorio, Matías Cavelli, Juan Pedro Castro-Nin, Diego Serantes, Alicia Costa, Giancarlo Vanini, George A. Mashour, and Pablo Torterolo. Urethane anaesthesia exhibits neurophysiological correlates of unconsciousness and is distinct from sleep. *The European Journal of Neuroscience*, 59(4): 483–501, February 2024. ISSN 1460-9568. doi: 10.1111/ejn.15690.

[77] Haruya Yagishita, Yuya Nishimura, Asako Noguchi, Yu Shikano, Yuji Ikegaya, and Takuya Sasaki. Urethane anesthesia suppresses hippocampal subthreshold activity and neuronal synchronization. *Brain Research*, 1749:147137, December 2020. ISSN 0006-8993. doi: 10.1016/j.brainres.2020.147137. URL `https://www.sciencedirect.com/science/article/pii/S0006899320304959`.

[78] Jose M. Hurtado, Leonid L. Rubchinsky, and Karen A. Sigvardt. Statistical Method for Detection of Phase-Locking Episodes in Neural Oscillations. *Journal of Neurophysiology*, 91(4):1883–1898, April 2004. ISSN 0022-3077. doi: 10.1152/jn.00853.2003. URL `https://journals.physiology.org/doi/full/10.1152/jn.00853.2003`. Publisher: American Physiological Society.